Size-frequency distribution of boulders >=7 m on comet 67P/Churyumov-Gerasimenko

Maurizio Pajola, Jean-Bapiste Vincent, Carsten Güttler, Jui-Chi Lee, Ivano Bertini, Matteo Massironi, E. Simioni, Francesco Marzari, Lorenza Giacomini, Alice Lucchetti, et al.

A&A 583, A37 (2015)
DOI: 10.1051/0004-6361/201525975

Astronomy & Astrophysics
Special feature

Rosetta mission results pre-perihelion

Size-frequency distribution of boulders ≥7 m on comet 67P/Churyumov-Gerasimenko

Maurizio Pajola[1], Jean-Baptiste Vincent[2], Carsten Güttler[2], Jui-Chi Lee[3], Ivano Bertini[1], Matteo Massironi[4], Emanuele Simioni[5], Francesco Marzari[6], Lorenza Giacomini[4], Alice Lucchetti[1], Cesare Barbieri[1,6], Gabriele Cremonese[7], Giampiero Naletto[8], Antoine Pommerol[9], Mohamed R. El-Maarry[9], Sébastien Besse[10], Michael Küppers[11], Fiorangela La Forgia[6], Monica Lazzarin[6], Nicholas Thomas[9], Anne-Thérèse Auger[12], Holger Sierks[2], Philippe Lamy[12], Rafael Rodrigo[13,14], Detlef Koschny[11], Hans Rickman[15,16], Horst U. Keller[17], Jessica Agarwal[2], Michael F. A'Hearn[18], Maria A. Barucci[19,20], Jean-Loup Bertaux[21], Vania Da Deppo[5], Björn Davidsson[15], Mariolino De Cecco[22], Stefano Debei[23], Francesca Ferri[1], Sonia Fornasier[19,20], Marco Fulle[24], Olivier Groussin[12], Pedro J. Gutierrez[25], Stubbe F. Hviid[26], Wing-Huen Ip[3], Laurent Jorda[12], Jörg Knollenberg[26], J.-Rainer Kramm[2], Ekkehard Kürt[26], Luisa M. Lara[25], Zhong-Yi Lin[3], Jose J. Lopez Moreno[25], Sara Magrin[6], Simone Marchi[27], Harald Michalik[28], Richard Moissl[10], Stefano Mottola[26], Nilda Oklay[2], Frank Preusker[26], Frank Scholten[26], and Cecilia Tubiana[2]

(Affiliations can be found after the references)

Received 26 February 2015 / Accepted 8 June 2015

ABSTRACT

Aims. We derive for the first time the size-frequency distribution of boulders on a comet, 67P/Churyumov-Gerasimenko (67P), computed from the images taken by the Rosetta/OSIRIS imaging system. We highlight the possible physical processes that lead to these boulder size distributions.
Methods. We used images acquired by the OSIRIS Narrow Angle Camera, NAC, on 5 and 6 August 2014. The scale of these images (2.44–2.03 m/px) is such that boulders ≥7 m can be identified and manually extracted from the datasets with the software ArcGIS. We derived both global and localized size-frequency distributions. The three-pixel sampling detection, coupled with the favorable shadowing of the surface (observation phase angle ranging from 48° to 53°), enables unequivocally detecting boulders scattered all over the illuminated side of 67P.
Results. We identify 3546 boulders larger than 7 m on the imaged surface (36.4 km^2), with a global number density of nearly 100/km^2 and a cumulative size-frequency distribution represented by a power-law with index of −3.6 +0.2/−0.3. The two lobes of 67P appear to have slightly different distributions, with an index of −3.5 +0.2/−0.3 for the main lobe (body) and −4.0 +0.3/−0.2 for the small lobe (head). The steeper distribution of the small lobe might be due to a more pervasive fracturing. The difference of the distribution for the connecting region (neck) is much more significant, with an index value of −2.2 +0.2/−0.2. We propose that the boulder field located in the neck area is the result of blocks falling from the contiguous Hathor cliff. The lower slope of the size-frequency distribution we see today in the neck area might be due to the concurrent processes acting on the smallest boulders, such as i) disintegration or fragmentation and vanishing through sublimation; ii) uplifting by gas drag and consequent redistribution; and iii) burial beneath a debris blanket. We also derived the cumulative size-frequency distribution per km^2 of localized areas on 67P. By comparing the cumulative size-frequency distributions of similar geomorphological settings, we derived similar power-law index values. This suggests that despite the selected locations on different and often opposite sides of the comet, similar sublimation or activity processes, pit formation or collapses, as well as thermal stresses or fracturing events occurred on multiple areas of the comet, shaping its surface into the appearance we see today.

Key words. comets: general – comets: individual: 67P/Churyumov-Gerasimenko – methods: data analysis

1. Introduction

On 6 August 2014, ESA's Rosetta spacecraft reached its primary target, the Jupiter-family comet 67P/Churyumov-Gerasimenko (hereafter 67P) at 3.60 AU from the Sun and 2.71 AU from Earth. The Optical, Spectroscopic and Infrared Remote Imaging System (OSIRIS) onboard Rosetta consists of a narrow- and a wide-angle camera (NAC and WAC) that are equipped with 26 medium- and narrow-band filters that cover the 240–1000 nm wavelength range (Keller et al. 2007). The NAC has a spatial scale of 18.8 cm/px when it is at 10 km from the surface, while the WAC reaches a resolution of 1.01 m/px at the same distance. Shortly after commissioning at the end of March 2014, OSIRIS has repeatedly acquired images of 67P (Mottola et al. 2014; Tubiana et al. 2015), resolving the nucleus in the NAC on 16 June 2014 at 192 000 km. After that, the resolution increased rapidly, reaching a scale of 18.6 cm/px during the ~10 km orbits around 67P performed at the end of October 2014.

The nucleus, its activity, and the surface morphology of 67P, as observed from OSIRIS cameras, are described in Sierks et al. (2015) and in Thomas et al. (2015b). Comet 67P is characterized by two main lobes: the larger one, hereafter the body, has dimensions of 4.1 × 3.3 × 1.8 km, while the smaller one, hereafter the head, is 2.6 × 2.3 × 1.8 km wide. The region located between the head and the body is 2.2 km long and roughly 0.8 km wide; it is hereafter called the neck. Comet 67P orbits the Sun every 6.5 years, it rotates around its axis with a period

Table 1. Power-law index for a variety of terrestrial fragmented objects according to Turcotte (1997).

Object	Reference	Power-law index
Artificially crushed quartz	Hartmann (1969)	−1.89
Disaggregated gneiss	Hartmann (1969)	−2.13
Disaggregated granite	Hartmann (1969)	−2.22
Broken coal	Bennet (1936)	−2.50
Projectile fragmentation of quartzite	Curran et al. (1977)	−2.55
Projectile fragmentation of basalt	Fujiwara et al. (1977)	−2.56
Sandy clays	Hartmann (1969)	−2.61
Soils	Wu et al. (1993)	−2.80
Terrace sands and gravels	Hartmann (1969)	−2.82
Glacial till	Hartmann (1969)	−2.88
Ash and pumice	Hartmann (1969)	−3.54

of 12.4043 ± 0.0007 h (Mottola et al., 2014), the rotational axis of the comet has an obliquity of 52°. At the time of this analysis, only two-thirds of the entire comet surface was observed, since the southern hemisphere was in shadow due to seasonal effects. To gain a complete view of the shadowed hemisphere, we have waited until comet equinox in May 2015. The mass of the comet is 1.0×10^{13} kg, and the density is 470 ± 45 kg/m^3 (Sierks et al. 2015).

One of the various morphological features characterizing the surface of 67P is the ubiquitous presence of large blocks (Thomas et al. 2015b). Boulders of various sizes are observed on asteroids and planets and are usually related to impacts; they are typically the largest fragments excavated by the collision that do not reach escape velocity after the impact. Blocks on asteroids have been described in detail by Lee et al. (1986) for Phobos and Deimos, by Geissler et al. (1996) and Lee et al. (1996) for (243) Ida, by Thomas et al. (2001) for (433) Eros, by Küppers et al. (2012) for (21) Lutetia, and by Michikami et al. (2008) for (25143) Itokawa. This is the first time, however, that boulders are observed on a cometary nucleus, thanks to the higher resolution of OSIRIS with respect to previous observations (which was 7 m at best for earlier datasets[1]).

Understanding the presence of boulders on comets is a challenge in itself because the impact formation process is not sufficient to explain them. Current collision rates for comets are very low (see Belton et al. 2013; Vincent et al. 2014) and would imply that most blocks were created very early in the history of the comet. If this were the case, a mechanism would be expected that preserved them on the surface for billions of years, but any long-duration mechanism is very unlikely to be effective because of the activity of comet surface and because of comet lifetimes (Kresak 1981; Levison & Duncan 1994). The following section of the paper describes this formation problem in detail and examines different mechanisms. In the subsequent sections, several questions related to the boulders observed on 67/P are considered, such as their evolution and their spatial and cumulative size-frequency distributions on the head, body, and neck, as well as in several localized areas. The naming convention used to identify the regions on 67P follows Thomas et al. (2015b).

[1] The previous best resolution (~7 m) obtained on a comet was achieved by the Deep Impact mission, renamed EPOXI, that flew by comet 103P/Hartley 2 on 4 November 2010 (A'Hearn et al. 2011). Before 103P/Hartley 2, the Deep Impact spacecraft observed comet 9P/Tempel 1 with a resolution of 10 m (A'Hearn et al. 2005). A few images were taken by the projectile on its way to the nucleus, with higher resolution (~3 m) but on a very limited area (~1 km^2). Nevertheless, the exact resolution is difficult to estimate because of the trajectory gave a very slanted view and the pixel scale varies across the image.

2. Boulder formation processes

Boulders are scattered all over the surface of 67P, they are ubiquitous on the head, neck, and body of the comet; they can be found both isolated or in clusters. They are often at the bases of scarps, large walls, or within terraces and well-delimited depressions. These distributions most likely depend on the formation process and evolution they have undergone. The present section discusses the different processes that may have formed the boulders seen on the comet surface on the bases of known studies about fragmentation and boulder field genesis on Earth and minor bodies of the solar system, by accounting for their observed locations and predictable size-frequency distributions. Since the surface of a comet is an active and changing environment, multiple boulder formation processes are expected to be at work, such as thermal stress fragmentation coupled with activity and jets, pit formation, gravitational phenomena, and possibly impacts. Moreover, if the gas drag force acting on the surface is similar to the gravity, the boulders seen at a given point of the surface might have been lifted from a different area and been redeposited on the surface, possibly undergoing fragmentation after landing.

2.1. Fragmentation on Earth: a frame context for interpreting cometary results?

On Earth, fractal fragmentation is commonly observed on impact shattering, explosive disruptions, crushed materials, weathered materials, and volcanic ejecta. A good discussion of such phenomena was presented by Turcotte (1997), who summarized the main power-law index values derived for different types of terrestrial fragmented objects from millimeter- to meter-sized fragments (see Table 1). Despite its obvious connection to the bulk density of terrestrial materials, which are not expected to be found on a comet, this table provides a first reference frame for understanding how one fragmentation process can result in a specific cumulative power-law index value. These values range between −2.0 and −3.0 when considering different types of deposits, as is the case for sandy clays and gravels or processes such as rock disaggregation and impact fragmentation. However, when fragments of ash and pumice are considered (Hartmann 1969), the slope of the cumulative size-frequency distribution increases to −3.54. We highlight this value for three main reasons: i) ash and pumice are possibly some of the closest matches to terrestrial material, at least for the density, that we can imagine are constituting the cometary nucleus; ii) the power-law index of this material is the closest to the one measured in specific comet locations, shown in Sect. 4, and finally; iii) ash and pumice are the typical product of explosive volcanism when fragmentation is related to subsurface volatile overpressure and release.

2.2. Fragmentation and sublimation

The surface of a comet is an active and changing environment. Rapidly mutable insolation conditions and associated thermal stresses together with outgassing of volatiles and dust from active areas can lead to pervasive cracks and fractures both on the cometary surface (Sierks et al. 2015; Thomas et al. 2015b) and on the single boulders. This implies that thermal stresses occurring on the comet surface can lead to cracks and fractures producing dislodged blocks as well as a continuous and quick fragmentation of boulders, as can be seen in Fig. 1A and B, which provides strong evidence of heavily fractured boulders surrounded by broken material that once might have been part of the boulders themselves. Moreover, although most of the boulders on the comet display an albedo and colors similar to the rest of the surface, some few boulders shows highly reflective patches with a distinctly bluer spectrum on their surfaces. If these bright meter-sized boulders (or bright patches located on larger boulders) are made of H_2O ice (Pommerol et al. 2015), they are expected to soon be affected by sublimation (and hence fracturing while 67P approaches the Sun). The boulders we detect on the surface may consist of dust components mixed with different super-volatile material, which together with the sublimation can justify the active sublimating or fragmenting boulders and the consequent plethora of meter-sized boulders that we see all over the surface of 67P. Fragmentation by thermal stress and sublimation activity can be two of the main causes that mutually increase the population of smaller boulders with respect to larger boulders and eliminate the smaller blocks by reducing them into dust or grains. The first effect results in a steepening of the size-frequency slope, while the second tends to make the slope fainter. Moreover, we need to distinguish whether the generation of the deposit is an episodic event that occurs only once and is followed by the boulder population evolving, or if the generation of the deposit is a continuous event and occurs on the same timescales as the erosion of blocks. In the latter case, we have a quasi-stationary state that can occur if the same mechanisms (thermal stresses and sublimation) cause the cliffs to disaggregate. The consequence of this is that the slope of the distribution is not expected to change because the boulders are replenished at all scales and a steady state is reached. It is therefore important to understand which of the two effects dominates for each boulder deposit.

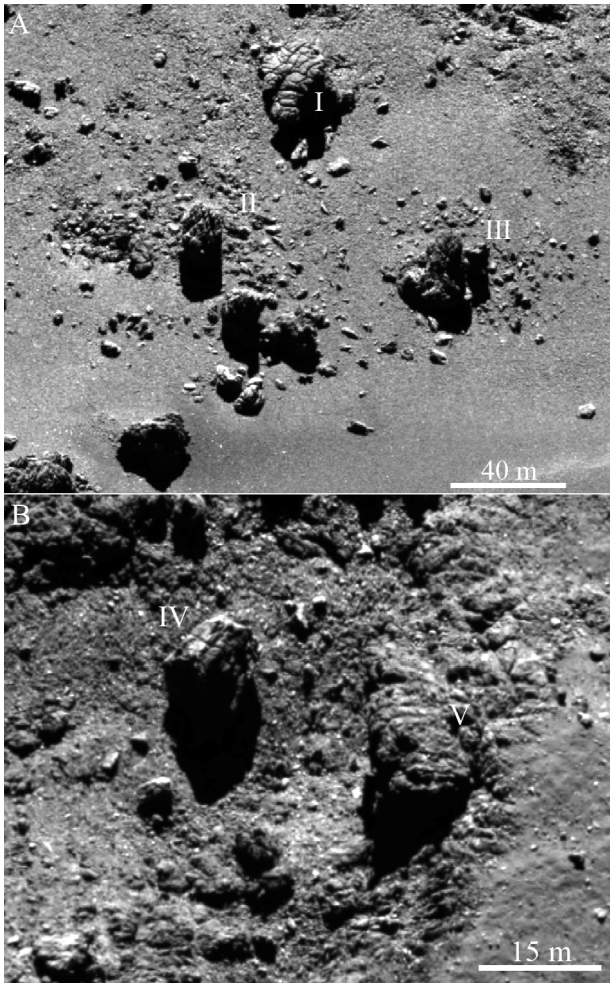

Fig. 1. A) OSIRIS NAC image (see Table 6 for image ID) taken on 29 November 2014 at a distance of 16.94 km from the surface of 67P. The scale of the image is 0.32 m/px. This area is located in the Imhotep region (Thomas et al. 2015b); I is a 30 m boulder crossed by multiple fractures, i.e., a good candidate for future fragmentation. II and III show examples of split materials located around an 18 m boulder (II) and a 34 m boulder (III). **B)** OSIRIS NAC image taken on 22 October 2014 at a distance of 8.10 km from the surface of 67P. The resolution of the image is 0.15 m/px. IV and V are 10 m boulders with multiple fractures surrounded by split material.

2.3. Outbursts and gravitational falls

The numerous scarps dominated by niches and terraces (see, e.g., the Seth region studied in Massironi et al. 2015) with localized debris fields at their bases suggest that gravitational phenomena induced by differential erosion are the dominant process on comet 67P. In particular, a differential regressive erosion by sublimation on a layered sequence might affect strata with different content of material that is prone to volatilization (higher erosion for layers with materials that are prone to become volatile). Figure 2 shows a model of scarp evolution affected by differential sublimation and gravitational falls. Underlying volatile-rich strata at the base of a layered sequence might start sublimating, thus favoring the collapse of the uppermost strata. If the active spots do not produce outburst, new niches and more cuesta margins are formed (D1, in Fig. 2), with a resulting accumulation deposit at the base of the receding walls. Conversely, if an outburst occurs, it can eject some or all of the boulders, eroding a large area of the cliff and favoring possible new gravitational collapses that may trigger new sublimation by again exposing the uppermost strata (D2, in Fig. 2). This origin may be well representative for most of the clustered gravitational falls we see inside the pits of Seth (with dimensions between 0.05–0.20 km^2), as seen in Fig. 3A.

Moreover, there may be some other areas, such as Imhotep or Hatmehit, where collapses of wider (0.4–0.6 km^2) areas as a result of outgassing on the underlying strata may have occurred in the past. We suggest that the boulders located at the center of these wide depressions are representative of the remnant part of the roof top layers or surface area, whereas at the margin of these depressions are deposits related to gravitational phenomena and differential regressive erosion by sublimation, Fig. 3B. Taluses at the depression margins are most probably continuously refurbished by blocks and grains from the nearby cliffs (as for the Seth pits), whereas deposits with boulders located at the center of the depression are most likely related to the previous genesis of the depression through a roof-collapse phase, hence they are older and not renewed. We suggest that these latter deposits probably underwent a longer period of activity and sublimation.

Table 2. Power-law index for asteroids visited by space missions.

Object	Mission	Reference	Power-law index	Diameter size
(433) Eros	NASA/NEAR	Thomas et al. (2001)	−3.2	≥15 m
		Dombard et al. (2010)	−3.1	≥1 m
(25143) Itokawa	Jaxa/Hyabusa	Michikami et al. (2008)	−3.1 ± 0.1	≥5 m
		Mazrouei et al. (2014)	−3.5 ± 0.1	≥6 m
(21) Lutetia	ESA/Rosetta	Küppers et al. (2012)	−5.0	≥60 m

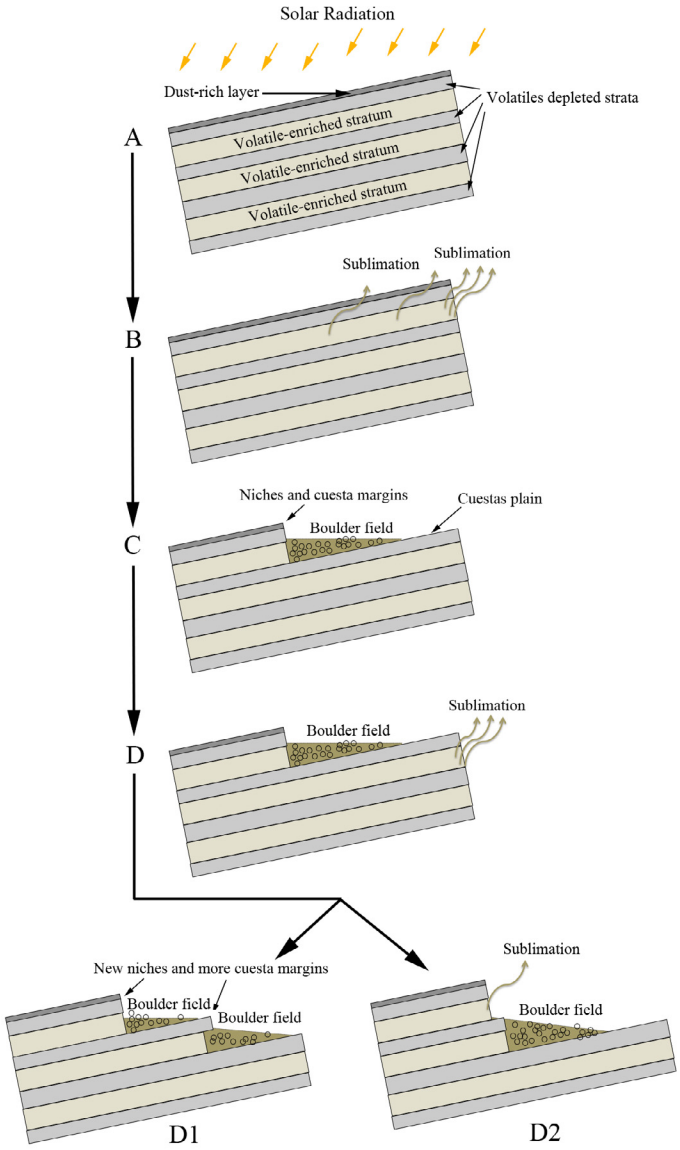

Fig. 2. Section of the comet showing the stratified structure of alternatingly enriched and depleted volatile strata. The four different steps show an occurring collapse triggered by activity with the following production of a boulder field or multiple boulder fields at the base of the receding walls.

2.4. Impacts

Boulders or large blocks on asteroids are mainly interpreted as resulting from impact processes. They are the largest fragments excavated during the impact and are typically found within the crater or in its close vicinity because they have not reached the escape velocity. As retained ejecta fragments, these blocks give information on the impact cratering processes on bodies with

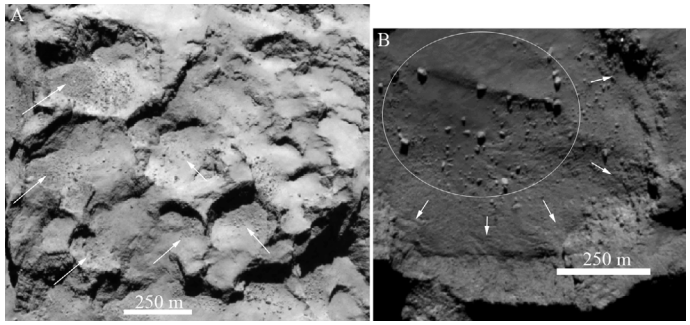

Fig. 3. A) Subframe of a NAC image (see Table 6 for image ID) taken on 6 August 2014. Pits in the Seth region are indicated with white arrows together with the corresponding gravitational falls. **B)** Subframe of a NAC image taken on 6 August 2014 showing a subsection of the Hatmehit depression. At its center, the boulders representative of the remnant part of the past surface area are indicated with the white circle. At the margin of this depression (white arrows) there are deposits related to gravitational phenomena and differential regressive erosion by sublimation.

low gravity (Lee et al. 1996). Deriving boulder-size distributions has been an important scientific topic addressed in several fly-by and orbital missions to asteroids. The first studies were performed by Lee et al. (1986) for Phobos and Deimos and by Geissler et al. (1996), who detected 17 positive reliefs with size between 45 and 150 m on the main-belt asteroid (243) Ida using NASA/Galileo observations. The NASA/NEAR mission orbited the near-Earth asteroid (433) Eros. The collected images allowed Thomas et al. (2001) to detect ~7000 rocks larger than 15 m over the entire surface, while a later analysis allowed investigating ~34 000 boulders larger than 1 m (Dombard et al. 2010). Michikami et al. (2008) found 373 boulders larger than 5 m on the near-Earth asteroid (25143) Itokawa by using images taken by the JAXA/Hayabusa mission. In a successive measurement, Mazrouei et al. (2014) counted 820 rocks with a major axis larger than 6 m. Using ESA/Rosetta data, Küppers et al. (2012) found more than 200 boulders with sizes in the 60−300 m range on the surface of the large main-belt asteroid (21) Lutetia. Carsenty et al. (2014), using orbital data from the NASA/Dawn mission, detected ~5000 boulders larger than 60 m on the surface of the main-belt asteroid (4) Vesta. A summary of the cumulative boulder-size distribution power-law index measured on asteroid surfaces from in situ data is shown in Table 2. The few values given in this table range from −3.1 to −3.5, with the exception of 21 Lutetia, for which the resolution was much poorer than for Eros and Itokawa, however. These counts were performed with resolutions reaching size-limits of 1 to 15 m, while for Lutetia only boulders larger than 60 m could be taken into account.

On the surface of 67P there is only evidence for a single impact crater of 30 m (Thomas et al. 2015b). Another possibility is that a specific location at the head, called Hatmehit, is the result of an ancient impact, but this is discussed below. Recent

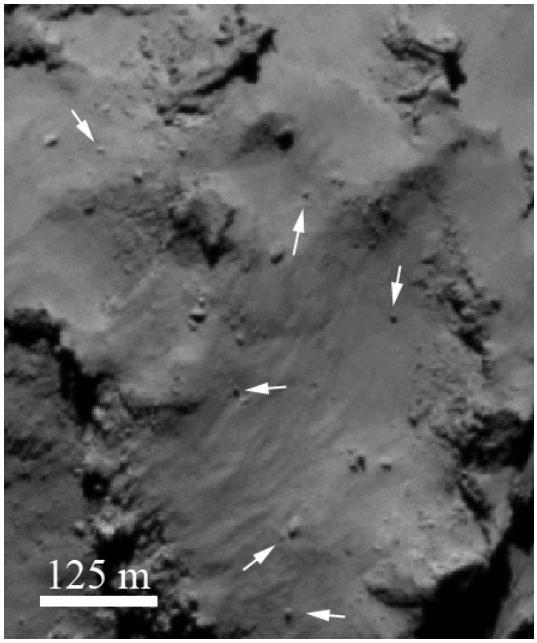

Fig. 4. Example of single isolated boulders (indicated with white arrows) located in the Ma'at region, which were probably lifted from the surrounding areas and eventually landed here. This is a subframe of a NAC image (see Table 6 for image ID) taken on 6 August 2014 at a distance of 119.3 km from the surface of 67P. The scale of the image is 2.2 m/px.

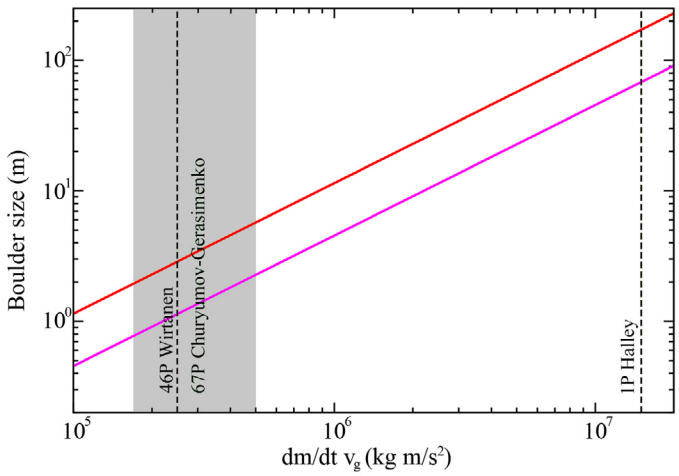

Fig. 5. Largest boulder size that can be lifted by outgassing as a function of the comet activity expressed as $\mathrm{d}m/\mathrm{d}t v_g$, where v_g is the gas velocity at the surface and $\mathrm{d}m/\mathrm{d}t$ is the local gas-loss rate. The purple line shows the largest diameter for the highest surface gravity that can be encountered on the surface of 67P, while the red line outlines the largest boulder size when the lowest gravity of 67P is considered. The outgassing values for comet 46P Wirtanen and 1P Halley are presented together with the range (gray) of $\mathrm{d}m/\mathrm{d}t v_g$ for 67P following Bertaux et al. (2014).

statistical studies have shown that even for Jupiter-family comets crossing the main belt every few years, the probability of an impact between an asteroid and a cometary nucleus is very low. Belton et al. (2013) and Vincent et al. (2014) have estimated that of all circular features observed on comets, less than 4%[2] can realistically be due to impacts. The situation was of course different at the time of comet formation, beyond the orbit of Neptune, where the environment was much more favorable for collisions[3]. It is difficult, however, to understand how boulders that were created 4.5 billion years ago can survive many perihelion passages and be observable now, when most of the comet surface has been heavily changed by activity and the detected boulders seem to be affected by active fracturing (Fig. 1). Hence, it is reasonable to discard the impact origin for the boulders, and invoke different processes.

2.5. Lifting boulders

Isolated boulders are seen in several locations, such as in Ma'at (Fig. 4), Seth, Aker, and Babi. These boulders might have been lifted by cometary activity after a former fragmentation (Pommerol et al. 2015; Thomas et al. 2015a) and their flight terminated because of a change in the gas density or velocity in a different location with respect to the cradle where they formed.

To understand the largest dimension possible for a boulder that can be lifted from the surface of the comet, we have to consider the local surficial gravity field, taking into account the centrifugal force and the drag force produced by the outflowing gas triggered by sublimation processes. The gas drag force, $F_G D$, can be computed from Stokes' formula as

$$F_G D = M_b * a = \frac{C_D}{2} s^2 v_g \left(\frac{\mathrm{d}m}{\mathrm{d}t}\right)_g \frac{1}{r^2}, \quad (1)$$

where M_b is the mass of the boulder, a is the acceleration, C_D is the drag coefficient, s is the radius of the boulder, v_g is the gas velocity ($\sim$1 km s^{-1}), $(\mathrm{d}m/\mathrm{d}t)_g$ the gas-loss rate, and r is the cometocentric distance (Fulle 1997). When the drag force is similar to gravity, the boulder can take off. Its subsequent landing is determined by changes in the local mass-loss rate or anisotropies in the gravity field that can change the balance between $F_G D$ and gravity force, F_G. In Fig. 5 the largest size of the boulders that can be lifted is given as a function of the product of the mass-loss rate and gas velocity. We consider an interval of values for $v_g\,(\mathrm{d}m/\mathrm{d}t)_g$ ranging from that of comet 46P/Wirtanen (2.5×10^5 kg m/s^2, Crifo & Rodionov 1996, at 1.1 AU to that of 1P/Halley at 0.9 AU 1.5×10^7 kg m/s^2, Krankowsky et al. 1986).

By taking into account both the range of $v_g\,(\mathrm{d}m/\mathrm{d}t)_g$ for 67P (Bertaux et al. 2014) and considering the lowest and highest gravity of the comet, we derive from Fig. 5 that the largest size of liftable boulders is between 2 and 6 m. This agrees with the satellite analysis reported by Bertini et al. (2015), which presents no detections of objects larger than a few meters in the vicinity of the nucleus or in the orbit of 67P.

Another aspect that has to be studied when considering lifted boulders, or boulders falling from cliffs, is the subsequent impact at the end of the lifting process, or cliff fall, that might possibly induce further fragmentation. What happens if a boulder is lifted and falls back to the surface with a certain velocity?

[2] This number depends on the residence time in the main belt.

[3] Davis & Farinella (1997) modeled the collisional evolution of the Edgeworth-Kuiper Belt (EKB) and argued that all bodies that are like the Jupiter-family comets (JFC) (≥km size) are the product of collisions between larger objects. More recent studies like the Nice model (Gomes et al. 2005) estimate that the EKB, birth place of comets, has lost 90% of its mass during the migration of giant planets about 3.9 Ga ago, and therefore the chances of collisions were much higher in the early ages of the solar system. However, this early environment remains much less understood than the asteroid belt, and it is difficult to estimate the collision rate reliably.

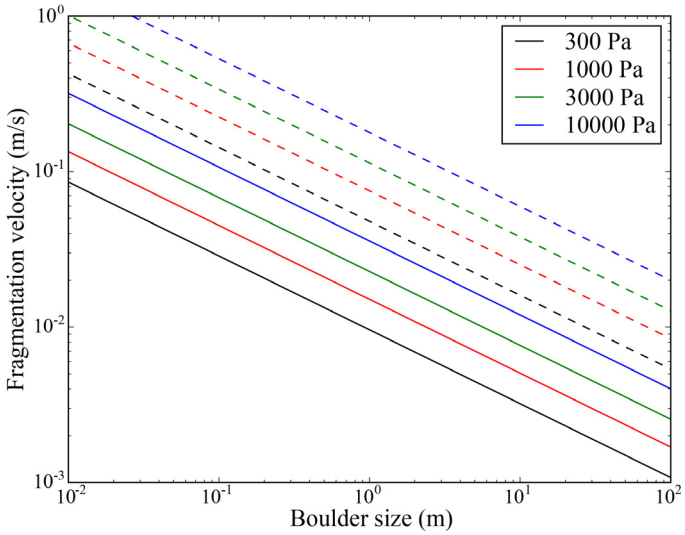

Fig. 6. Fragmentation velocity as a function of the boulder size for a range of reasonable tensile strengths based on Eq. (2). The solid lines show the onset of fragmentation ($\mu = 1.0$, where μ is the fragmentation strength), while the dashed lines show what is generally referred to as catastrophic fragmentation ($\mu = 0.5$), i.e., where the boulder breaks into many pieces, the largest of which contains half of the boulder's original mass.

The breakup of porous, very fragile aggregates of different sizes was studied by Beitz et al. (2011). In their case, the aggregates were centimeter-sized and possessed a tensile strength of typically 1000 Pa. After comparing these to literature data of different sizes, they provided a size-dependent breakup velocity given by their Eq. (14). When their scaling for the tensile strengths is included, this yields

$$v_{\rm break} = \sqrt{\left(4 * \left(\frac{T}{1000\ {\rm Pa}}\right)^{0.75} * \left(\frac{s}{34\ {\rm micron}}\right)^{-0.95}\right)}, \quad (2)$$

where $v_{\rm break}$ is the breakup velocity, T is the boulder's tensile strength, and s is the boulder size, that is, the diameter. The trend of these results is well established (e.g., Benz & Asphaug 1999), while the absolute velocity for fragmentation is one of the lowest measured because of the low tensile strength. Applied to the breakup of boulders on 67P, Fig. 6 shows the fragmentation velocity as a function of the boulder size for a range of reasonable tensile strengths following Eq. (2). The bulk tensile strength of 67P is given by Groussin et al. (2015), their highest value is 300 Pa. Since the boulders stand out morphologically, it is reasonable to assume that they are stronger than the bulk material so that we consider values of up to 10 000 Pa still possible. The solid lines in Fig. 6 show the onset of fragmentation, while the dashed lines show a stronger fragmentation, where the mass of the largest fragment is equal to half of the mass of the original boulder; this is generally referred to as catastrophic fragmentation. If we consider velocities between 0.1 m/s (a boulder that jumps or falls 50 m) and 0.9 m/s (representative escape velocity, Sierks et al. 2015), we see that boulders larger than 10 cm break for even a strength of 10 000 Pa, larger or weaker boulders experience much stronger fragmentation. We thus conclude that boulders break apart when they are significantly moved on the surface of 67P. It should be noted that the experiments of Beitz et al. (2011) are extrapolated by at least a factor of 5 in size, and their size dependance of the fragmentation velocity is stronger than in previous publications (Benz & Asphaug 1999). However, the conclusion is clear enough: only the smallest size of breaking boulders changes with this uncertainty. It might also be argued that the surface material into which the boulders impact can be much weaker, such that a significant amount of the impact energy is dissipated in the compaction of surface material, as was observed in the experiments of Langkowski et al. (2008). It is not observed that the boulders significantly penetrated the surface, however, so that we consider this a minor contribution.

It is not yet clear which power-law index can be representative of these lifted and possibly fallen and fragmented boulders; nevertheless, Kelley et al. (2013) presented the distribution of large particles observed in the coma of comet 103P/Hartley 2. Since these particles are much larger than the 0.1−100 μm sizes that are usually considered in comet dust, which reach dimensions of between 0.1 and 2.21 m (a few of the largest particles reach effective radii close to 4 m), their size-frequency distribution can be compared to the present results that were derived from the surface of the comet, which means that we view our results in a wider context. The power-law slope computed by Kelley et al. (2013) for this range of sizes is −4.7. This value can be considered as a fundamental first hint of the power-law of lifted particles or boulders that did not fall again and escaped from the surface of a comet. On one side, the steep behavior can be mainly caused by smaller particles being more easily lifted than larger boulders, and hence the depletion of larger particles steepens the slope toward smaller sizes. A second explanation of this trend is that these particles originated from superficial collapses with a subsequent escape of high-pressure volatiles and consequent high fracturing of larger boulders, again with the consequent steepening of the power-law distribution toward smaller sizes. Comet 103P/Hartley 2 is hyperactive (A'Hearn et al. 2011), hence it is hardly comparable to 67P. Nonetheless, the lifting-process phenomenon on 67P will be increasingly important when the comet approaches the Sun and consequently increases its activity. Future observations will place more constraints on this discussion and the possible power-law index of large meter-sized particles either present in the coma of 67P or fallen back onto its surface.

3. Dataset and methodology

On 5 and 6 August 2014, ESA's Rosetta spacecraft completed its rendez-vous with comet 67P and entered the comet orbit on 6 August at 09:06 UT. During the final approach, the dataset obtained by OSIRIS/NAC was of unprecedentedly high resolution, down to 2 m, imaging in full-frame mode (2048 × 2048 pixels) the comet nucleus during an entire 12.4 h rotation. These images were the highest resolution NAC exposures covering the full 67P nucleus and are of extreme importance to perform global studies of the surface and to define the physiographical regions of the body (El-Maarry et al. 2015).

The dataset we used in this work to derive the cumulative size-frequency distribution of the 67P boulders is presented in Table 3.

The distances given in Table 3 refer to the center of the ~4 km comet, not to the distance between the spacecraft and the foreground surface. However, a difference of ±2 km, which is the largest surface distance from the comet center, affects the scale of the foreground and background boulders by no more than 4 cm/px. In other words, at a distance of 120 km from the surface, a difference of 2 km results in an error of 1.67%, that is, 0.4 m for a 10 px (22 m) boulder. For the aim of this paper, we therefore consider this error negligible, since we use bins of 1 m to calculate the size-frequency distributions. It is more important

Table 3. OSIRIS NAC images used in this work.

Day	UT	Distance from 67P center (km)	Scale (m/px)
05-08-2014	19:43	131.5	2.4
05-08-2014	21:43	126.9	2.4
05-08-2014	23:20	123.5	2.3
06-08-2014	01:20	119.3	2.2
06-08-2014	02:20	117.2	2.2
06-08-2014	04:20	113.4	2.1
06-08-2014	06:20	109.8	2.0

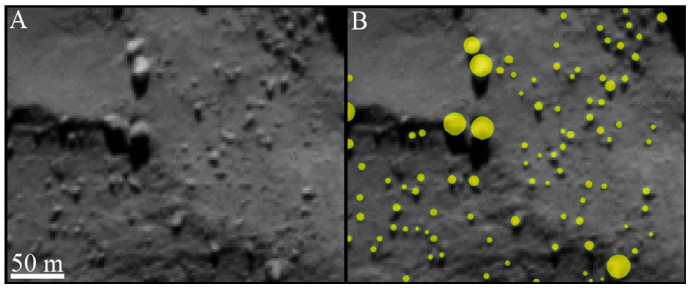

Fig. 7. Example of the methodology used to identify the boulders on the surface of comet 67P. **A)** Subframe of a NAC image (see Table 6 for image ID) taken on 6 August 2014 at a distance of 119.3 km from the surface of 67P. The scale of the image is 2.2 m/px. **B)** The same image with the detected boulders indicated in yellow circles are presented.

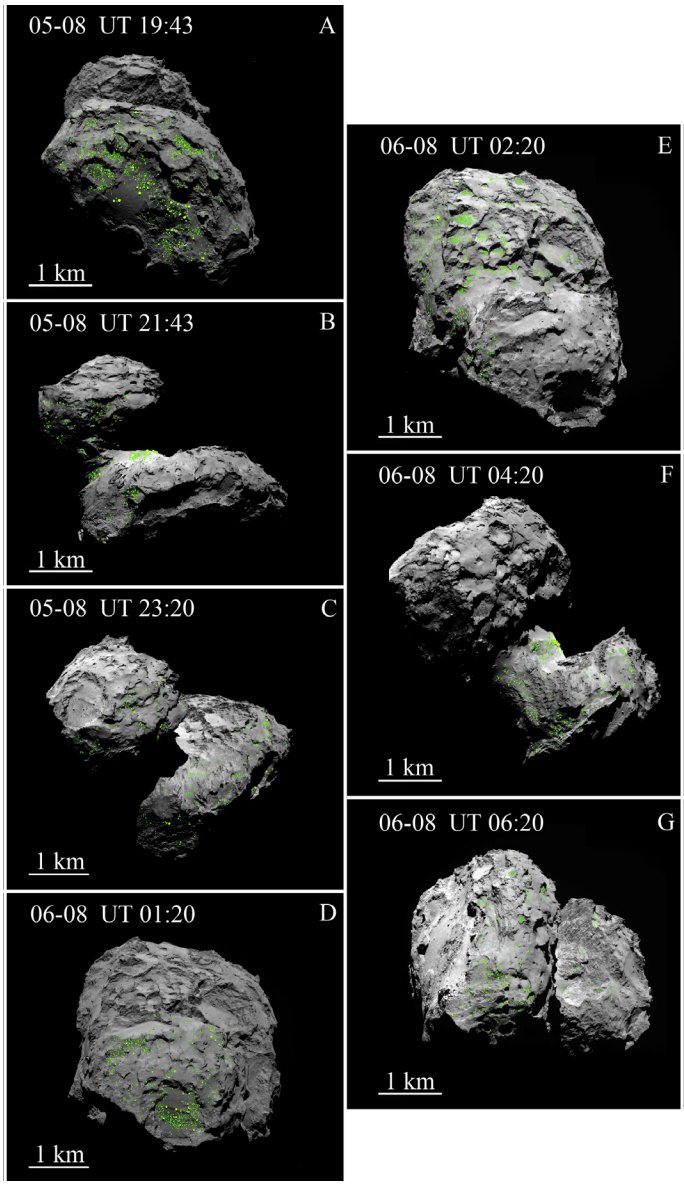

Fig. 8. Spatial distribution of the ≥7 m boulders on the illuminated side of 67P (75% of the total surface, equivalent to 36.4 km^2), derived from NAC images (see Table 6 for image ID) presented in Table 3.

to take into consideration the difference in scale between the first image of the dataset and the last one, which is 41 cm/px. To obtain a homogeneous dataset, we decided to consider as statistical meaningful boulders with a diameter larger than 7 m, that is, at least a three-pixel sampling, which minimizes the likelihood of misidentifying what we are detecting (Nyquist 1928). The value of 7 m derives from the image with the lowest resolution, which is the one obtained on 5 August at 19:43 UT. Since the observations were performed with an average phase angle of 50°, the presence of elongated shadows on the surface provides the possibility of identifying even smaller boulders (two pixels in diameter, ∼4−5 m). However, we decided to exclude these smaller boulders in the cumulative size-frequency distribution. Finally, we defined which features of the images we considered as "boulders". A "boulder" is a positive relief detectable in multiple images obtained with different observation geometries, with the constant presence of an elongated shadow (if the phase angle is greater than 0°) whose extension depends on the illumination geometry; moreover, a boulder seems to be "detached" from the ground where it stands. Once these features were manually identified in the high-resolution images, we measured their position on the surface of the comet, and assuming their shapes to be circumcircles, we derived their maximum length, that is, the diameter, and the corresponding area (Fig. 7). To obtain the cumulative boulder size-frequency distribution per km^2, we then used the corresponding area computed from the 3D shape model of 67P (Sierks et al. 2015).

4. Results

4.1. Global distributions

Boulders are ubiquitous on the head, neck, and body of 67P, but the largest of them, with diameters of about 50 m, are located on the neck and in the Imhotep region. The initial count was of 4976 boulders, reduced to 3546 for statistical purposes taking into consideration only those with a diameter larger than 7 m. Of the discarded 1430 smaller boulders, 602 fall in the 6−7 m bin, 587 are between 5 and 6 m, 222 between 4 and 5 m, and the remaining 19 are inside the 3−4 m bin. Figure 8 shows the spatial distribution of boulders on 67P.

The cumulative boulder size-frequency distribution per km^2 of the entire illuminated side of the comet was then derived by

Table 4. Names of the different regions, their area from the 3D shape model, the total number and surface density of boulders ≥7 m, power-law index, and associated error.

Name	$Area_{3D}$ (km^2)	Tot # boulders ≥7 m	# 7 m boulders per km^2	Power-index	+	–
All	36.4	3546	97	−3.6	0.2	0.3
Body	22.5	2218	99	−3.5	0.2	0.3
Head	10.8	1115	103	−4.0	0.3	0.2
Neck	3.1	213	69	−2.2	0.2	0.2

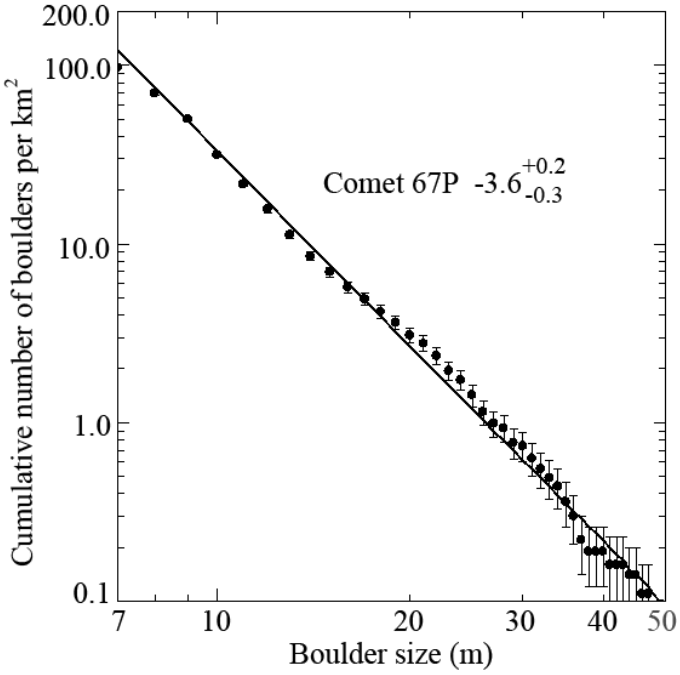

Fig. 9. Cumulative size-frequency distribution of boulders ≥7 m per km^2 over the illuminated surface of 67P. Vertical error bars indicate the root of the cumulative number of counting boulders (as from Michikami et al. 2008) divided by the illuminated area of 67P. The continuous line is a fitted regression line to the data, and the power-law index of the size distribution is −3.6 +0.2/−0.3. The bin size is 1 m.

considering the surface area of the comet shape model of 67P, which is 36.4 km^2 (Sierks et al. 2015). The resulting plot is presented in Fig. 9: the power-law index value is −3.6 +0.2/−0.3[4]. We then performed the same analysis by considering the body, head, and neck of the comet as separate regions to understand if there is any size-frequency difference between them. The body has an illuminated surface of 22.5 km^2, the head covers 10.8 km^2, while the neck alone has a surface of 3.1 km^2. As seen from Table 4, the total number of boulders ≥7 m belonging to the body is 2 218, while it is 1115 on the head and 213 for the neck. In Table 4 we summarize the corresponding values of the slope and power-law index for the entire illuminated side of 67P, its two main lobes and the neck, while their cumulative size-frequency distributions per km^2 are presented in Fig. 10.

[4] We here highlight that the regression line used to detect the power-law index fits the binned values that are ≥7 m, but does not take into account those points that are equally cumulatively repeated. When subsequent values present the same cumulative number, this is an indication of a poor statistics that has not to be considered by the fit. Such effect typically occurs at the bigger boulder sizes, as it is clear from Figs. 9, 10 and 12. This is valid for all plots presented in this work. Moreover, we underline that when evenly spaced horizontal bins are considered for the fit in the logarithmic representation, no significant power-law index changes are present (they are well within the error bars here presented), hence the 1 m size bin power-law indices can be considered a valid representation of the statistics.

4.2. Interpretation of the global distributions

The slopes of the cumulative distributions per km^2 of the body and head only slightly overlap (Table 4) if the error bars are taken into consideration, while this is not the case for head, body, and neck. Nevertheless, the largest number of boulders with a diameter larger than 7 m does not substantially differ between the body and the head of 67P; there are almost 100 boulders per km^2. The neck has only 69 boulders per km^2. Since there are no mineralogical differences between the body and the head (Capaccioni et al. 2015), but only slightly different slopes in visible wavelengths and specifically on the neck/Hapi (Fornasier et al. 2015; La Forgia et al. 2015), we can assume that the body and the head of 67P consist of the same material. How can we then explain a power-law index difference between the head and the body, if similar processes, that is, sublimation, jet-activity, thermal stresses, and gravitational falls (Vincent et al. 2015; Lin et al. 2015; Keller et al. 2015), occur on their surfaces?

Assuming that the boulders originated from the same processes on the head and body, the boulder size-distribution power-law index is most likely related to the fracture density of the intact mass from which these boulders were detached. Hence, higher values are probably representative of a more pervasive fracturing, and the higher size-distribution slope of the head of 67P implies a higher fracture density than in the body. This agrees with the surface observation at least of the exposed walls of the Seth and Hathor regions, which are good examples of the head and body (see also Massironi et al. 2015). Therefore, similar processes occurring on the surface are expected to produce a steeper global size-frequency distribution on the head than on the body because of the pre-existing fracture density. Nonetheless, specific localized areas both on the head and body show similar trends, as we present in section on the localized size-frequency distributions. In contrast, the neck of the comet (called Hapi) shows a trend that is different from the body and head, which means that a different interpretation is required to explain the −2.2 power-law index (Table 4). To support the hypothesis that the origin of the neck boulders is the fall of debris from the Hathor region, we examined the blocks in the heavily fractured and layered cliff or Hathor region (1.81 km^2 wide) that have not yet been dislodged, see Fig. 11. We used a NAC image, taken on 7 August 2014 at UT 20:37:34 at a distance of 81.57 km from 67P center with a scale of 1.54 m/px, which provides a good view of the region. The derived cumulative size-frequency distribution per km^2 has a very steep power-law index of −5.2+0.5/−0.6, see Fig. 12; this is completely different from the power-law index on the neck. On the other hand, the number of 7 m boulders on Hathor is 150, that is, about twice as many as identified on Hapi. At first glance, both the size-frequency

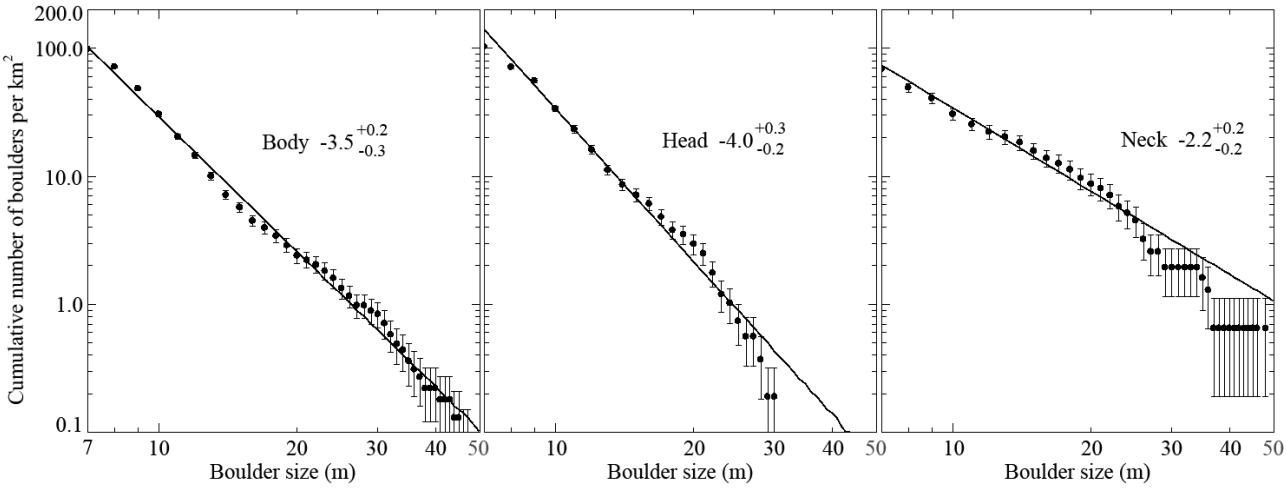

Fig. 10. Cumulative size-frequency distribution of ≥7 m boulders per km^2 on the body, head, and neck.

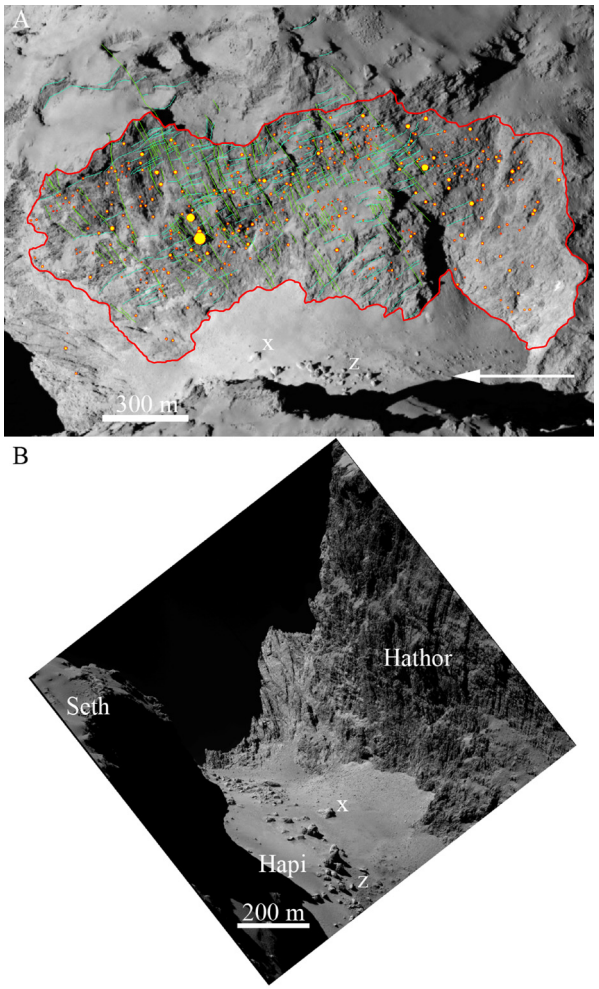

Fig. 11. A) Hapi (neck) and Hathor (cliff) regions with the identified blocks in yellow circles between terraces, fractures, and lineaments. The scale of this image (see Table 6 for image ID) is 1.54 m/px. The light blue lines identify the layers detected on the body, while the green lines identify the fractures crossing the cliff. The boulders are highlighted with yellow circumcircles with red borders. The white arrow shows the line-of-sight direction of image **B). B)** Side view of the neck with a scale of 0.53 m/px. This image was taken on 22 September 2014 at a distance of 28.24 km from the comet, and it is presented to show the field of boulders on the neck together with the debris below the Hathor cliff and Seth. Two boulders, called X and Z, are indicated in both figures. (See Fig. 20 Anaglyph.)

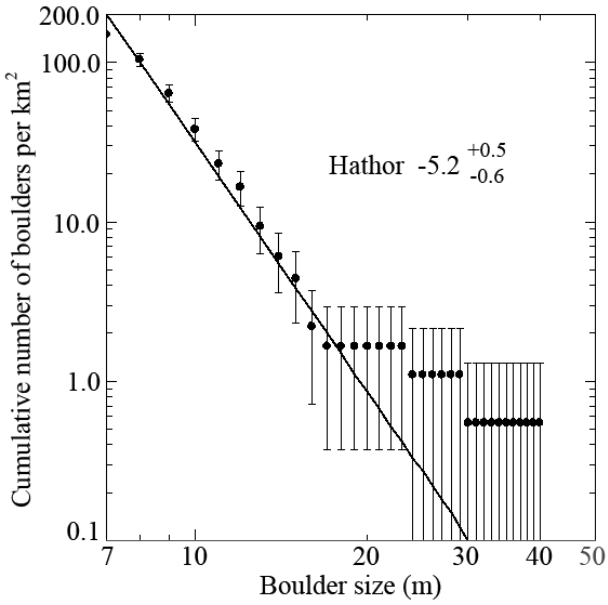

Fig. 12. Size-frequency distribution per km^2 on the Hathor fractured cliff. The poor statistics were enhanced by the 1 m binning for boulders larger than 18 m. These values cannot be considered in the fit, as explained in footnote 4.

distribution and the large number of small blocks on Hathor might therefore suggest that the boulders on the neck cannot be the result of blocks that fell from Hathor. But the gravity vectors on the cliff show that any block detached from Hathor will eventually fall down into the Hapi region (see Fig. 13), hence the distribution of boulders on Hapi most likely is the result of a modification of the size-frequency distribution of blocks visible on Hathor. In particular, what we see on the neck surface can be explained by invoking three different (but not mutually exclusive) effects, triggered by sublimation:

– The neck region is the first and most active region of the northern hemisphere of the comet (Sierks et al. 2015; Lin et al. 2015). Activity and jets coming from this region have been unequivocally detected since the end of July 2014 (3.66 AU), both from Hapi and Hathor. The past and present activity that has affected this area could be the main responsible factor for the decreasing cumulative size slope to

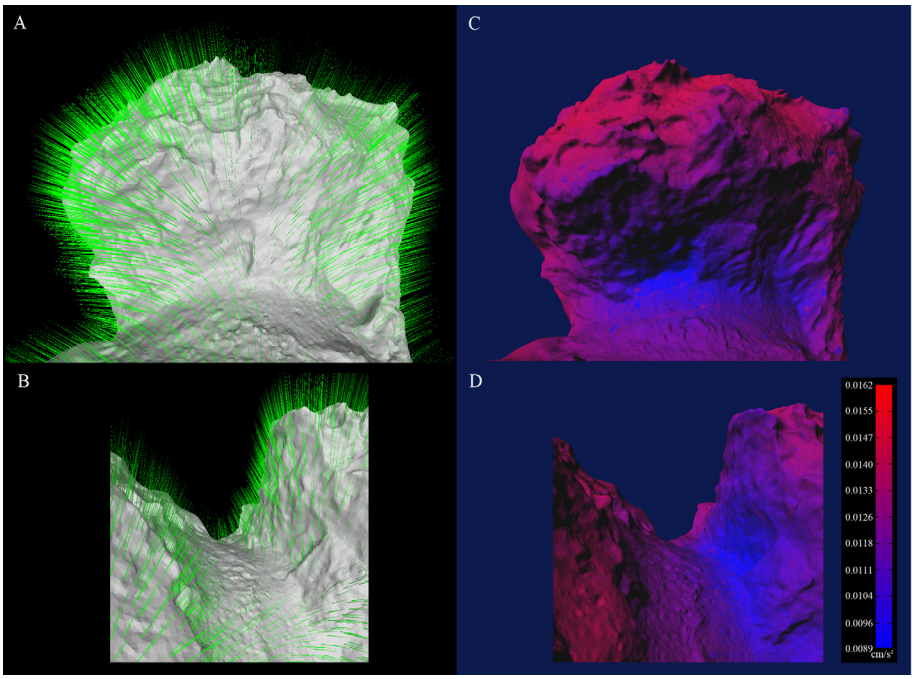

Fig. 13. Hapi (neck) and Hathor (cliff) regions with the gravity vectors displayed as green lines (**A)** and **B)**) and the local value of gravitational acceleration (that takes into account the centrifugal force) (**C)** and **D)**) with the same observation geometry as Fig. 11A and B.

the present values, since the smaller boulders were completely disintegrated or fragmented and disappeared through sublimation.

- Another possibility is that the activity that occurred on Hathor and Seth (this is the cliff opposite to Hathor, confining Hapi) can produce dusty materials that by falling down the cliff might bury the smaller boulders that are located on the neck. Figure 11B provides evidence of this, since most of the large boulders seem to be partially or almost completely buried by a brittle or dusty blanket, and very few small boulders are visible. Figure 11A and B clearly show that large boulders on the order of decameters are visible and almost aligned along the neck, whereas deposits hide boulders at the foot of the fractured Hathor wall and leave only the larger boulders uncovered.
- The third possibility is that the smaller boulders could have been lifted up and been redistributed to other areas (Thomas et al. 2015a) or been dispersed away from the comet into space if the drag force produced by the outflowing gas triggered by sublimation processes overcame the local surface gravity field. At the time of writing, dust grains on the order of centimeters are observed to leave the comet (Rotundi et al. 2015), hence if the drag force will grow with approach to perihelion, the lifting of boulders might become a possibility (see Sect. 2.5 on lifting boulders).

These scenarios would all result in some decrease of smaller boulders with respect to larger boulders, which would reduce the cumulative size-frequency power-law index value to the value we see on Hapi.

4.3. Size-frequency distributions in localized areas

We then focused on localized areas of the body and head that contained a significant amount of boulders larger than 7 m. The purpose of this analysis is to understand how the size-frequency distribution slopes differ when considering specific geomorphological contexts and possible different origins of boulder deposits. In particular, we identified two regions on the body: region 1, which consists of three areas that are representative of the layered or niche region of Seth and Ash (Massironi et al. 2015), and region 2, consisting of one depression on Ash, a smooth region inside Imhothep (Auger et al. 2015), and a layered region in Khepry. In addition to the blocks of the Hathor layered region presented above, we focused on the talus of the depressions of Nut and Hatmehit on the head (El-Maarry et al. 2015; La Forgia et al. 2015). The areas we identified clearly present defined morphological borders (Giacomini et al., in prep.), so that representative size-frequency statistics can be extracted. To derive the cumulative boulder size-frequency distribution per km^2, we made use of the corresponding area computed from the 3D shape model of 67P (Thomas et al. 2015b).

4.3.1. Body region 1 size-frequency distributions

The first area we examined is the Seth layered region (described in detail in Massironi et al. 2015), where multiple niches, strata heads, terraces, and cuesta margins are present. The first size-frequency distribution we derived is the one of area A, with a surface of 4.96 km^2 (Fig. 14). This area mainly shows two types of terrains: a rough layered region with niches (collapsed pits?) and cliffs, and a layered terrain mainly dominated by terraces covered by smooth deposits. Inside the multiple pits that can be identified in this area, there are diverse accumulation deposits. This area provides evidence of regional (Lin et al. 2015; Keller et al. 2015) and localized sublimation activities (Vincent et al. 2015): the power-law index that we derive from the cumulative size-frequency distribution per km^2 is −4.2 +0.7/−1.1 (see Fig. 15A). In greater detail within the major pits of this region, that is, B and C in Fig. 14, the detected boulders show a size-frequency distribution with power-law index values of −6.5 +0.3/−0.4 and −5.8 +0.3/−0.5 (see Fig. 15), the first value is the highest measured on the entire comet.

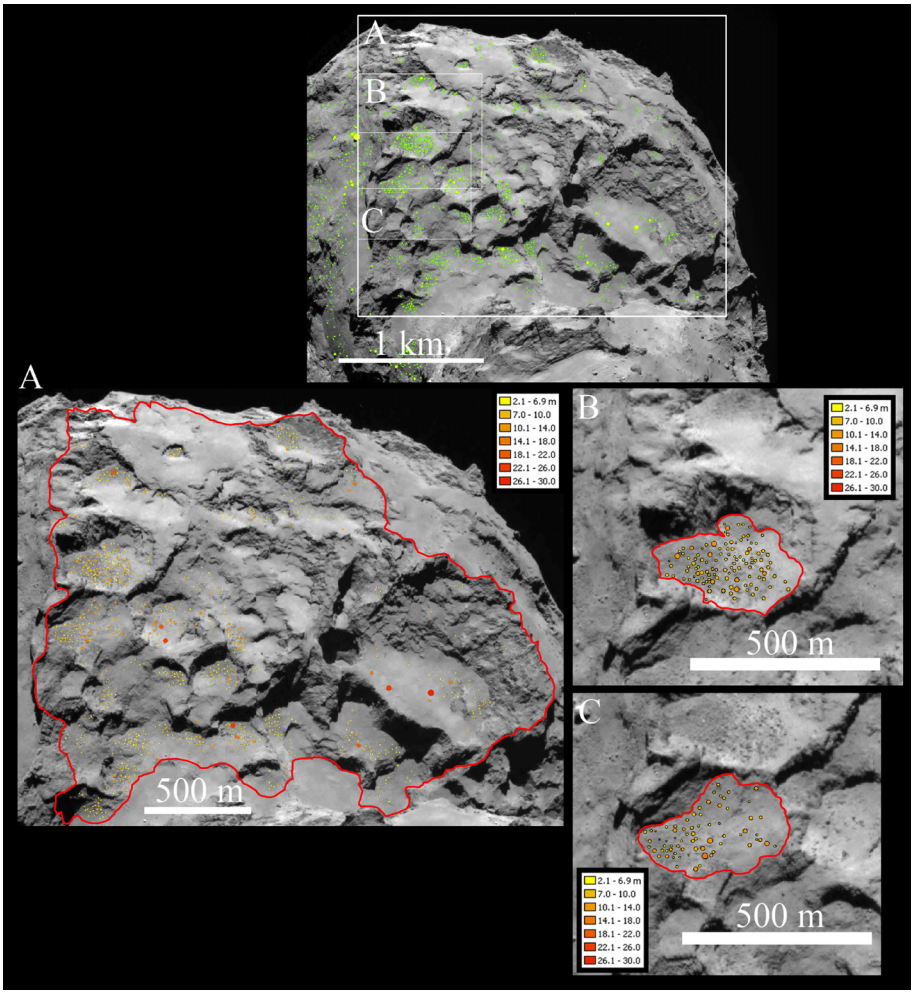

Fig. 14. Three localized areas studied on Seth and Ash. A is 4.96 km^2 wide; B has a surface of 0.10 km^2; while C is 0.08 km^2 wide (see Table 6 for image ID).

4.3.2. Body region 2 size-frequency distributions

The second set of areas we considered is presented in Fig. 16, where main units are visible: a region dominated by a smooth background (A), a layered region with a large niche and two step-like terraces (B), and a wide elongated depression (C). Area A is located within the smooth region of Imhotep (Auger et al. 2015) and is a 0.19 km^2 wide elliptical depression bordered on one side by a prominent scarp underlined by talus deposits at its base. Smooth deposits with boulders are located close to the scarp and within the depression, while a flat area without boulders is located on the lower right side of the depression. The size-frequency distribution per km^2 of this area shows two different trends, the first one (between 7 and 11 m) with a power-law index value of −3.6 +0.1/−0.2 and the second one (between 11 and 15 m) of −1.0 +0.1/−0.1, see Fig. 17I. The probability density distribution, Fig. 17II, shows that this composite distribution is due to the bimodal boulder distribution, which increases toward smaller boulders and stops at the resolution detection limit (7 m), and a peak centered on ∼15.5 m. Area B (0.29 km^2 wide) is located between Ash and Khepry: it appears to be a gravitational deposit most probably detached by the large arched niche. The derived power-law index of this boulder size-frequency distribution is −3.8 +0.1/−0.2 (Fig. 17III), highly coherent with the talus and gravitational deposits of site A. The third area, C, is a talus deposit 0.16 km^2 wide, located inside an elongated asymmetrical depression on a broad terrace bordered by a layered scarp on one side. The power-law index we identified on this size-frequency distribution is −6.4 +0.3/−0.4, which is extremely close to the one derived from the boulder accumulation in area B of Fig. 14.

4.3.3. Head size-frequency distributions

The last two areas we analyzed are located on the head of 67P. The first one, A, is the gravitational deposit lying inside Nut, which is a depression with a surface of 0.17 km^2. The cumulative size-frequency power-law index per km^2 we derived for this boulder talus is −3.9 +0.3/−0.2. In contrast, area B of Fig. 18, called Hatmehit, is an almost circular depression, 0.49 km^2 wide and with a diameter of ∼0.9 km with a depth-to-diameter ratio of ∼0.2 (La Forgia et al. 2015). Its rim shows evidence for large-scale collapses and fracturing. The floor of the depression is flat and smooth, seemingly covered with material far smaller than the resolution limit of our images. A step crosses its surface passing throughout a smooth terrain with unevenly distributed boulders (175 blocks larger than 7 m). For this area we derived a bimodal trend of the boulder distribution similar to the one identified in the Imhothep/body 2 area A (Fig. 16). It shows two power-law index values: −3.4 +0.2/−0.1 (between 7 and 13 m), and −1.0 + 0.1/−0.2 (between 13 and 22 m), see Fig. 19II. The probability density distribution, Fig. 19III, shows that this composite distribution is due to the bimodal boulder distribution that increases toward smaller boulders and stops at the resolution detection limit (7 m), and a peak centered on ∼22.5 m.

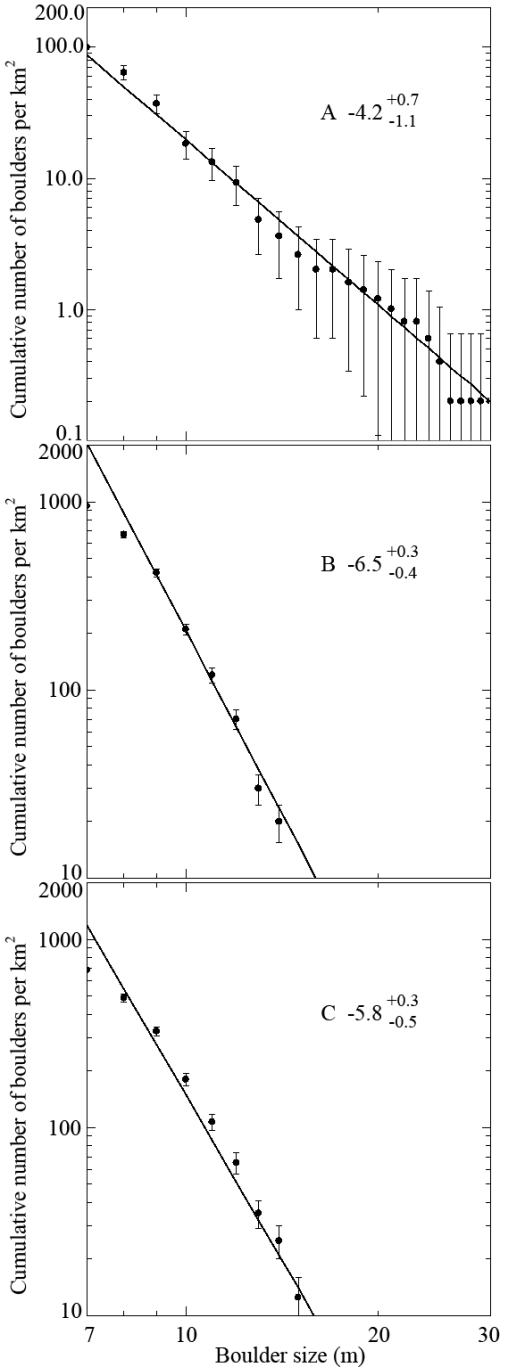

Fig. 15. Size-frequency distributions for area A on Seth and Ash and the two circular pits on Seth, B and C, presented in Fig. 14.

4.4. Interpretation of the results on localized areas

To summarize, in Table 5 we present all power-law index values we obtained on eight specific locations of comet 67P. These regions can be subdivided as follows:

- Body 1 A region encloses rough layered cliffs with frequent niches and large terraces covered by smooth layered terrain with deposits of boulders. It generally shows a size-frequency distribution with a power-law index of −4.2. The slope of this entire area A is lower than the specific pit locations (body1 B, C), which is probably caused by the contribution of boulders generated by gravitational processes alone and not necessarily also by jet activity and sublimation processes.
- Three pit regions (i.e., body 1 B, body 1 C, and body 2 C) are characterized by a power-law index ranging from −5.8 to −6.5 and corresponding error bars that overlap partially, if not entirely. This is an indication of high fragmentation, probably due to their genesis, which is related to jet activity and a recent or still active sublimation. The origin of these pits can be explained by roof collapses induced by sublimation of subsurface layers, possibly accompanied by short-lived mini-outbursts (Vincent et al. 2015). After formation, these pits can expand in diameter through sublimation and retreat from their enclosing walls. Sublimation and gravitational falls most likely control the wall retreat; the walls might eventually collapse. The final result is that the floors of enlarged and collapsed pits are covered by dust and debris falling from the enclosing walls. The steep power-law indices we see in these areas can be related to the concurring effect of gravitational collapses plus local activity and jets during boulder genesis and thermal stress fragmentation. The activity and subsurface volatile outflow might possibly induce additional steepening of the power-law indices with respect to the distribution simply related to gravitational processes. Moreover, the boulders located in the pits are not equally distributed on the floor (see Figs. 14B and C), but instead seem clustered close to decametric-high cliffs, where the lowest gravity potential within the pits is centered. Despite its elongated shape driven by a morphological control, the third pit (body 2 C) presents a boulder deposit similar to the two main pits (body 1B and C) located on Seth. Hence, it is possible that the boulders located inside this area (Fig. 16C) are the result of the same sequence of collapse, sublimation, and gravitational processes affecting the Seth region.
- The depressions of body 2 A (Imhotep) and head B (Hatmehit) show a composite distribution with two power-law indices: a first one ranging between −3.6 and −3.4 and a second one with a slope of −1.0. This composite distribution is due to the bimodal boulder distribution, as the probability density of these two depressions shows (Figs. 17II and 19III). A possible explanation of this behavior is that there are two different types of deposits within these areas. Talus deposits bordering the scarp progressively degrade into smooth deposits with larger boulders in the center of the depression (see Fig. 3B). This terrain is then followed by smooth deposits without boulders. Hence, we suggest that the dichotomy of the size-frequency distribution can be explained by two different deposits with boulders, that is, talus deposit at the depression margins and smooth terrain with boulders within the center of the depression. The latter typology could be representative of the remnant part of the extended collapse of the entire area. After the original collapse, the whole area could have undergone areal sublimation and regressive erosion at the bordering cliffs. The final result could have been a dismantling and elimination of smaller boulders in the central part of the depression and a progressive erosion and retreat of the surrounding walls with production of talus debris continuously renovated by blocks and grains. As we explained in Sect. 2.2, sublimation acts on one hand by fragmenting the larger boulders into their constituting elements (see Figs. 1A and B), while on the other hand it eliminates smaller blocks. The first effect results in a steepening of the size-frequency slope, while the second tends to lower it. The fact that the older deposits

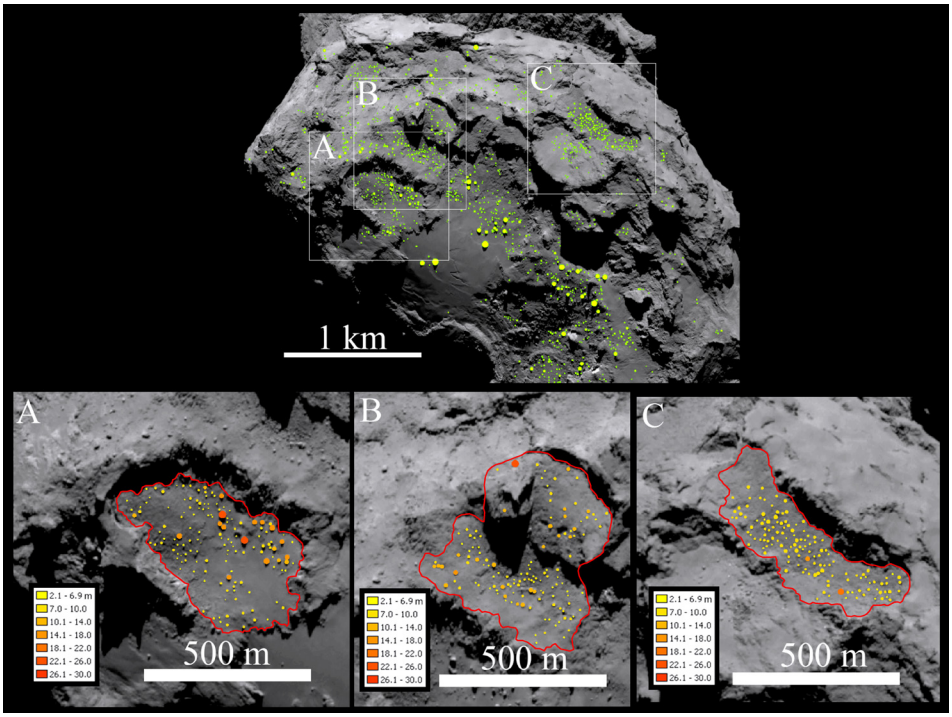

Fig. 16. Three localized areas studied on Imhotep, Ash, and Khepry (see Table 6 for image ID).

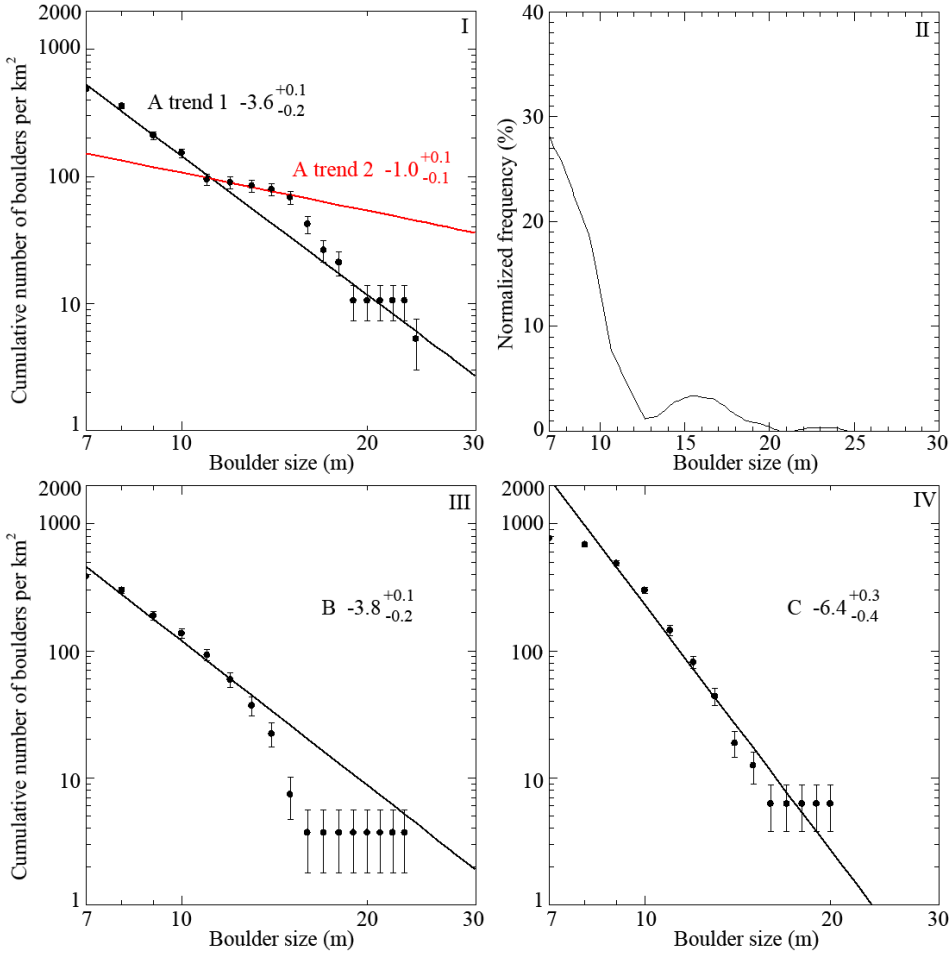

Fig. 17. Size-frequency distribution per km^2 of area A presented in Fig. 16. **II)** The continuous frequency percentage of the boulder sizes for area A, evaluated as the derivative of the cumulative distribution of the boulders cleaned with a low-pass filter and normalized to the total amount of the boulders considered. **III)** and **IV)** size-frequency distributions per km^2 for areas B and C.

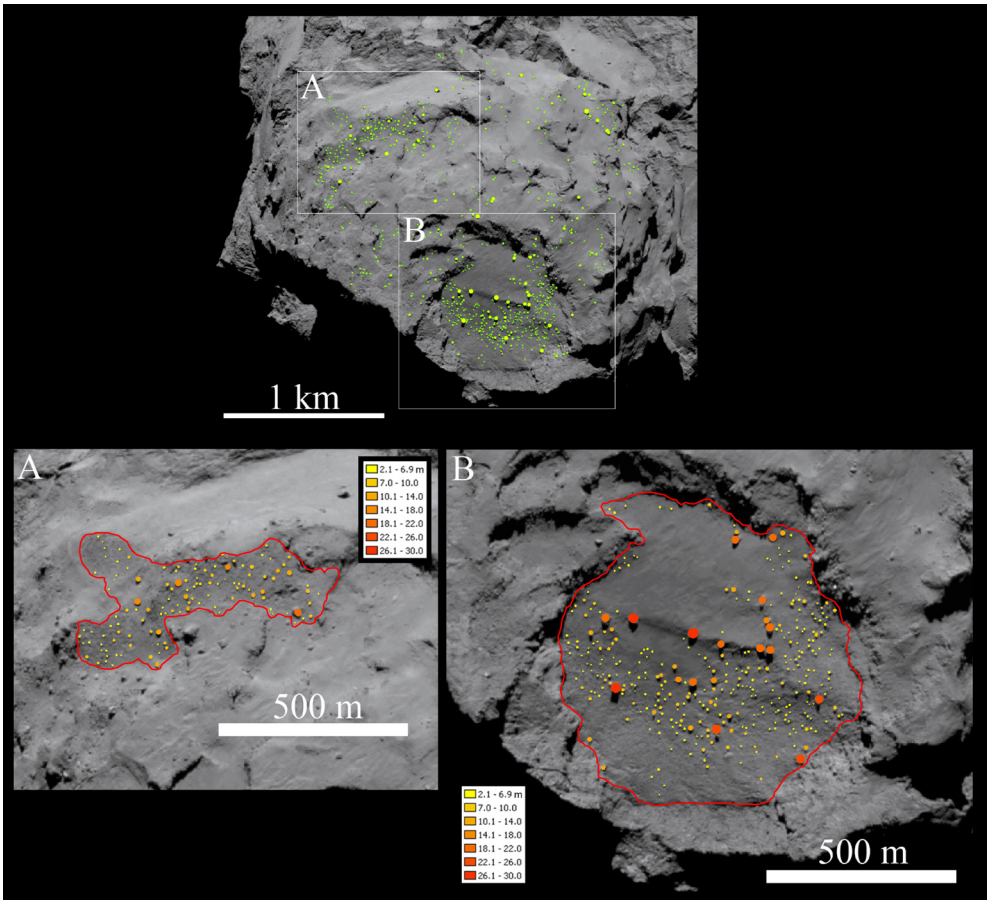

Fig. 18. Two localized areas studied on Nut and Hatmehit (see Table 6 for image ID).

located at the center show lower slopes than the sideward repeatedly renewed deposits is an important hint that fragmentation of larger boulders is dominant at an early stage of the deposit generation and development, whereas disappearance through sublimation of smaller boulders becomes much more relevant at later stages and longer periods. In this view, Hatmehit or head B could be the widest area on the comet where this type of collapse could have occurred in the past.

Although there is no evidence for impact craters on 67P (with the one exception of a 30 m crater located in the Ash region, see Thomas et al. (2015b), the idea that an ancient impact may have shaped the Hatmehit region cannot be excluded a priori. The largest fragment here presents measures of about 30 m in diameter. The cumulative size distribution of these blocks has a slope equal to −3.4, possibly compatible with an impact origin. Scaling laws have been derived from the study of lunar craters and experiments on Earth and established an empirical link between several physical properties of the target and projectile. It is generally assumed that the size of the largest fragment follows the power-law $D_{\rm L} = 0.25\ D_{\rm crater}^{0.7}$ with $D_{\rm L}$ the size of the largest fragment and $D_{\rm crater}$ the diameter of the crater in meters (Lee et al. 1996). This scaling law is derived for possibly much stronger material than what is found on a comet, but it has also been validated for more porous objects such as the asteroid Eros (Thomas et al. 2001), on which boulders could be unambiguously linked to the Shoemaker crater. When applying this equation to the Hatmehit region, we derive a largest size of 31 m, which is compatible with the size of blocks we observe. While this result is remarkable, we need to be cautious because of the large uncertainty on the material properties of the comet (Hatmehit seems to be an area that is less active, and it has higher thermal inertia than other regions (Gulkis et al. 2015; Capaccioni et al. 2015) indicating compacted material) and because there is multiple evidence, as presented above, that point toward a collapse origin. Nevertheless, a full understanding of the area and final arguments regarding an impact origin require extensive modeling and experiments and is beyond the scope of this paper.

– Gravitational taluses are present in the regions of body 2 B and head A. The first region is located at the boundary between Khepry and Ash, the second one is on Nut. Although the two regions belong to opposite sides of the comet, they both show similar power-law indices ranging between −3.8 and −3.9. It is important to note that this distribution is similar to the steeper trends derived from the taluses located at the two depressed regions presented above.

We summarize our results to interpret the boulder formation and evolution as follows:

1. Collapses/pit formation and creation of depressions with subsequent escape of high-pressure volatiles[5] and consequent high fracturing are characterised by power-law indeces of about −5 to −6.5.

[5] Belton (2010, 2014) and Belton et al. (2013) indicate that 81P/Wild 2 and 9P/Tempel 1 pits are sublimational or erosional pits caused by internal or outburst activity. It is therefore possible to infer that similar 67P/Churyumov-Gerasimenko pits underwent alike formation processes, and hence not being pristine.

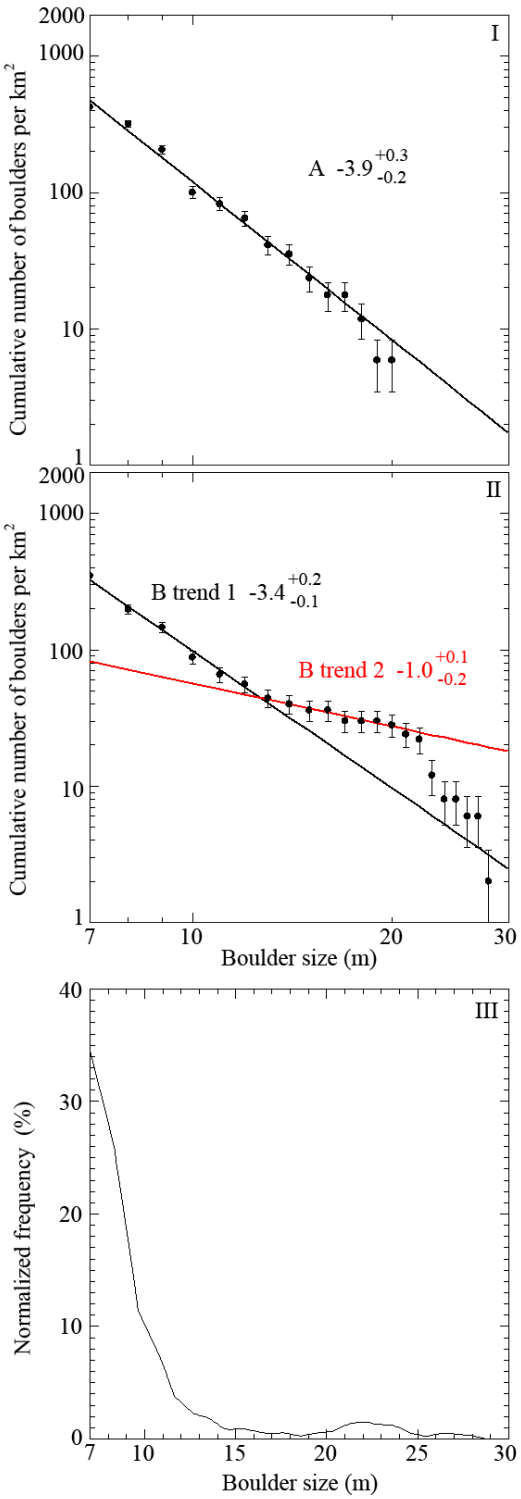

Fig. 19. Panels **I)** and **II)**: size-frequency distribution per km^2 of area A and B of Fig. 18. Panel **III)**: continuous frequency percentage of the boulder sizes, for area B, evaluated as the derivative of the cumulative distribution of the boulders cleaned with a lowpass filter and normalized to the total amount of the boulders considered.

2. Gravitational events triggered by sublimation and/or thermal fracturing causing regressive erosion present power-law indeces of about −3.5 to −4.
3. Evolution of the original material formed during both the collapsing or the gravitational event, not particularly renewed, or present in areas where continuous and high sublimation occurred or is still occurring show power-law indeces of about −1 to −2.

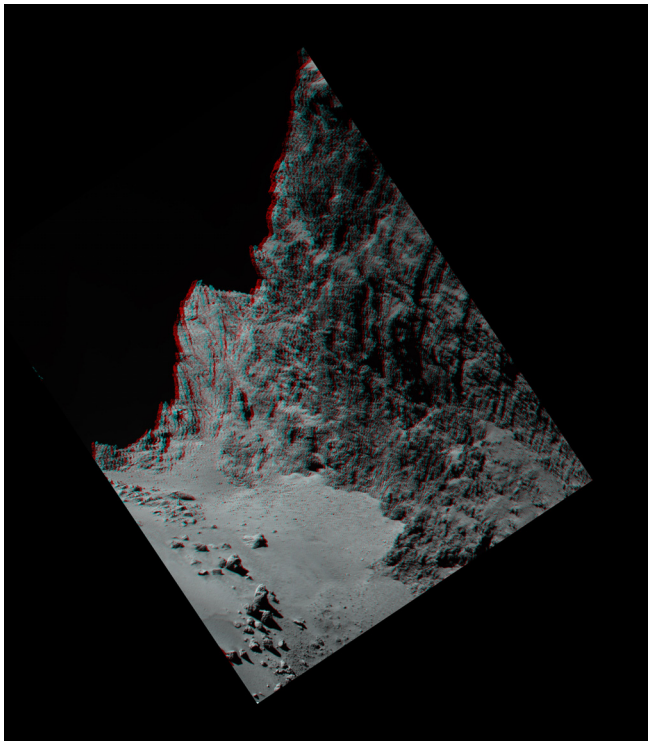

Fig. 20. Anaglyph version of Fig. 11B showing the fractured Hathor cliff and the boulders below (see Table 6 for image ID).

The global distribution of boulders shows that both head and body are mostly dominated by boulders of type 2, while the neck could be dominated by boulders of type 3. Boulders of type 1 (collapse or pit formation) possibly indicate recent or latest events, this is the reason why the global size-distribution is not dominated by these power laws. In these cases collapse occurred, but sublimation as well as wall regression have not yet been dominant, nor the diffuse sublimation.

It is worth noting that such similar distributions are derivable from different and often opposite sides of the comet (head and body of 67P). This is an important hint that despite the different global distributions we found on the head and the body of the comet, specific deposits in akin geomorphological settings show similar cumulative boulder size distributions. This validates the possibility that similar processes occurred and likely will occur in the next future on both lobes of comet 67P while the comet is approaching perihelion in August 2015.

5. Conclusion

We presented the first size-frequency boulders distribution per km^2 of a comet, 67P/Churyumov-Gerasimenko, measured on ESA Rosetta/OSIRIS images of the nucleus. We derived the global size-frequency distribution of boulders larger than 7 m measured on the entire illuminated side of the nucleus, and subsequently focused on the different distributions of the two lobes into which the nucleus is divided and on the region that connects them. The slopes of the cumulative distributions per km^2 between the body and head only partially overlap, while there is no overlap between them and the neck. Since the boulder size-distribution power-law index is a measurement of the degree of

Table 5. Power indices of the slope of the cumulative boulder size-distribution per km^2 of localized areas on comet 67P.

Name	Geographical unit	Area$_{3D}$ (km^2)	# 7 m boulders per km^2	Power-law index	+	–
Body1 A	Seth/Ash	4.96	100	−4.2	0.7	1.1
Body1 B	Seth	0.10	950	−6.5	0.3	0.4
Body1 C	Seth	0.08	688	−5.8	0.3	0.5
Body2 A trend 1	Imhotep	0.19	485	−3.6	0.1	0.2
Body2 A trend 2	Imhotep			−1.0	0.1	0.1
Body2 B	Khepry/Ash	0.29	385	−3.8	0.1	0.2
Body2 C	Ash	0.16	769	−6.4	0.3	0.4
Head A	Nut	0.17	424	−3.9	0.3	0.2
Head B trend 1	Hatmehit	0.49	350	−3.4	0.2	0.1
Head B trend 2	Hatmehit			−1.0	0.1	0.2

Table 6. Figure number and corresponding image ID.

Figure	Image ID
1	A: NAC-2014-09-29T13.29.30.598Z-ID30-1397549600-F22.IMG
	B: NAC-2014-10-22T02.16.55.299Z-ID30-1397549700-F22.IMG
3	A: NAC-2014-08-06T02.20.12.490Z-ID30-1397549400-F41.IMG
	B: NAC-2014-08-06T01.20.12.587Z-ID30-1397549700-F41.IMG
4	NAC-2014-08-06T01.20.12.587Z-ID30-1397549700-F41.IMG
7	A: NAC-2014-08-06T01.20.12.587Z-ID30-1397549700-F41.IMG
	B: NAC-2014-08-06T01.20.12.587Z-ID30-1397549700-F41.IMG
8	A: NAC-2014-08-05T19.43.14.611Z-ID30-1397549000-F22.IMG
	B: NAC-2014-08-05T21.43.14.596Z-ID30-1397549900-F22.IMG
	C: NAC-2014-08-05T23.20.11.041Z-ID30-1397549300-F41.IMG
	D: NAC-2014-08-06T01.20.12.587Z-ID30-1397549700-F41.IMG
	E: NAC-2014-08-06T02.20.12.490Z-ID30-1397549400-F41.IMG
	F: NAC-2014-08-06T04.20.10.447Z-ID30-1397549800-F41.IMG
	G: NAC-2014-08-06T06.20.11.419Z-ID30-1397549200-F41.IMG
11	A: NAC-2014-08-07T20.37.34.564Z-ID30-1397549300-F22.IMG
	B: NAC-2014-09-22T08.51.16.356Z-ID30-1397549100-F22.IMG
14	NAC-2014-08-06T02.20.12.490Z-ID30-1397549400-F41.IMG
16	NAC-2014-08-05T19.43.14.611Z-ID30-1397549000-F22.IMG
18	NAC-2014-08-06T01.20.12.587Z-ID30-1397549700-F41.IMG
20	NAC-2014-09-22T08.51.16.356Z-ID30-1397549100-F22.IMG

fracturing, where higher values relate to stronger and more extended fracturing (i.e., more smaller than larger boulders), the head of 67P is generally more fractured than the body. This agrees with the surface observation at least of the exposed walls of the Seth and Hathor regions, which are well representative of the head and body and provide abundant hints on the inner structure of the comet nucleus. Therefore, similar processes occurring on the surface probably produce a steeper global size-frequency distribution on the head than on the body because of the pre-existing structural framework and fracture density. This seems to clearly explain the difference we found on the power-law index values. We then suggest that the boulder field located on the neck area is the result of blocks that fell from the contiguous Hathor cliff. Three different not mutually exclusive effects, triggered by sublimation, may have occurred on the neck, leading to the size-frequency distribution we see today: i) disintegration or fragmentation and disappearance through sublimation of the smallest boulders; ii) uplifting and consequent redistribution of the smallest boulders on the surface of 67P if the drag force produced by the outflowing gas triggered by sublimation processes overcame the local surficial gravity field; and iii) production of a dusty blanket that covers the smallest boulders close to the Seth and Hathor cliffs.

In addition to this, we derived the size-frequency distribution of localized areas on 67P. These areas are located on different and often opposite sides of the comet. Nevertheless, we obtained similar cumulative size-frequency distributions when similar geomorphological settings are present. This is an important indication that suggests that similar activity processes, pit formation or gravitational collapses and thermal fracturing events, most likely occurred in different areas of the comet, forming the size-frequency distributions we see today.

Acknowledgements. We thank the anonymous referee for important and constructive comments that lead to a substantial improvement of the paper. The identification of the boulders in high-resolution images has been one of the products required by the lander team to OSIRIS and has been accomplished by using OSIRIS NAC and WAC images. The position, surface, and largest size of each boulder located on the five proposed Philae landing sites, and specifically the two finalists (Agilkia and site C), were identified by Maurizio Pajola (UPD-Padova, Italy) and Jean-Baptiste Vincent (MPS-Göttingen, Germany). The final products were delivered to the lander team on 30 September 2014. OSIRIS was built by a consortium of the Max-Planck-Institut für Sonnensystemforschung, in Göttingen, Germany, the CISAS-University of Padova, Italy, the Laboratoire d'Astrophysique de Marseille, France, the Instituto de Astrofisica de Andalucia, CSIC, Granada, Spain, the Research and Scientific Support Department of the European Space Agency, Noordwijk, The Netherlands, the Instituto Nacional de Tecnica Aeroespacial, Madrid, Spain, the Universidad Politechnica de Madrid, Spain, the Department of Physics and Astronomy of Uppsala University, Sweden, and the Institut für Datentechnik und Kommunikationsnetze der Technischen Universität Braunschweig, Germany. The support of the national funding agencies of Germany (DLR), Italy (ASI), France (CNES), Spain (MEC), Sweden (SNSB), and the ESA Technical Directorate is gratefully acknowledged. We thank the ESA teams at ESAC, ESOC, and ESTEC for their work in support of the Rosetta mission. The team in Taiwan was supported by the Ministry of Science and Technology of Taiwan. We made use of the Arcgis 10.2 software together with IDL, Matlab, and R software to perform the presented analysis.

References

A'Hearn, M. F., Belton, M. J. S., Delamere, W. A., et al. 2005, Science, 310, 258
A'Hearn, M. F., Belton, M. J. S., Delamere, W. A., et al. 2011, Science, 332, 1396
Auger, A.-T., Groussin, O., Jorda, L., et al. 2015, A&A, 583, A35
Beitz, E., Güttler, C., Jorda, L., et al. 2011, ApJ, 736, 34
Belton, M. J. 2010, Icarus, 210, 881
Belton, M. J. S. 2014, Icarus, 231, 168
Belton, M. J. S., Thomas, P., Carcich, B., et al. 2013, Icarus, 222, 477
Bennet, J. G. 1936, J. Inst. Fuel, 10, 22
Benz, W., & Asphaug, E. 1999, Icarus, 142, 5
Bertaux, J.-L., Combi, M. R., Quémerais, E., & Schmidt, W. 2014, Planet. Space Sci., 91, 14
Bertini, I., Gutiérrez, P. J., Lara, L. M., et al. 2015, A&A, 583, A19
Capaccioni, F., Coradini, A., Filacchione, G., et al. 2015, Science, 347, 628
Carsenty, U., Wagner, R., Jaumann, R., et al. 2014, LPI Contributions, 1773, 2036
Crifo, J. F., & Rodionov, A. V. 1996, BAAS, 28, 1086
Curran, D. R., Shockey, D. A., Seaman, L., & Austin, M. 1977, in Impact and Explosion Cratering: Planetary and Terrestrial Implications, eds. D. J. Roddy, R. O. Pepin, & R. B. Merrill, 1057
Davis, D. R., & Farinella, P. 1997, Icarus, 125, 50
Dombard, A. J., Barnouin, O. S., Prockter, L. M., & Thomas, P. C. 2010, Icarus, 210, 713
El-Maarry, M. R., Thomas, N., Giacomini, L., et al. 2015, A&A, 583, A26
Fornasier, S., Hasselmann, P. H., Barucci, M. A., et al. 2015, A&A, 583, A30
Fujiwara, A., Kamimoto, G., & Tsukamoto, A. 1977, Icarus, 31, 277
Fulle, M. 1997, A&A, 325, 1237
Geissler, P., Petit, J.-M., Durda, D. D., et al. 1996, Icarus, 120, 140
Gomes, R., Levison, H. F., Tsiganis, K., & Morbidelli, A. 2005, Nature, 435, 466
Groussin, O., Jorda, L., Auger, A.-T., et al. 2015, A&A, 583, A32
Gulkis, S., Allen, M., von Allmen, P., et al. 2015, Science, 347, 709
Hartmann, W. K. 1969, Icarus, 10, 201
Keller, H. U., Barbieri, C., Lamy, P., et al. 2007, Space Sci. Rev., 128, 433
Keller, H. U., Mottola, S., Davidsson, B., et al. 2015, A&A, 583, A34
Kelley, M. S., Lindler, D. J., Bodewits, D., et al. 2013, Icarus, 222, 634
Krankowsky, D., Lammerzahl, P., Herrwerth, I., et al. 1986, Nature, 321, 326
Kresak, L. 1981, Bull. Astron. Inst. Czechosl., 32, 321
Küppers, M., Moissl, R., Vincent, J.-B., et al. 2012, Planet. Space Sci., 66, 71
La Forgia, F., Giacomini, L., Lazzarin, M., et al. 2015, A&A, 583, A41
Langkowski, D., Teiser, J., & Blum, J. 2008, ApJ, 675, 764
Lee, S. W., Thomas, P., & Ververka, J. 1986, Icarus, 68, 77
Lee, P., Veverka, J., Thomas, P. C., et al. 1996, Icarus, 120, 87
Levison, H. F., & Duncan, M. J. 1994, Icarus, 108, 18
Lin, Z.-Y., Ip, W.-H., Lai, I.-L., et al. 2015, A&A, 583, A11
Massironi, M., Simioni, E., Marzari, F., et al. 2015, Nature, submitted
Mazrouei, S., Daly, M. G., Barnouin, O. S., Ernst, C. M., & DeSouza, I. 2014, Icarus, 229, 181
Michikami, T., Nakamura, A. M., Hirata, N., et al. 2008, Earth Planets Space, 60, 13
Mottola, S., Lowry, S., Snodgrass, C., et al. 2014, A&A, 569, L2
Nyquist, H. 1928, Trans. Am. Inst. Elect. Eng., 47, 617
Pommerol, A., Thomas, N., El-Maarry, M. R., et al. 2015, A&A, 583, A25
Rotundi, A., Sierks, H., Della Corte, V., et al. 2015, Science, 347, 3905
Sierks, H., Barbieri, C., Lamy, P. L., et al. 2015, Science, 347, 1044
Thomas, N., Davidsson, B., El-Maarry, M. R., et al. 2015a, A&A, 583, A17
Thomas, N., Sierks, H., Barbieri, C., et al. 2015b, Science, 347, 440
Thomas, P. C., Veverka, J., Robinson, M. S., & Murchie, S. 2001, Nature, 413, 394
Tubiana, C., Snodgrass, C., Bertini, I., et al. 2015, A&A, 573, A62
Turcotte, D. L. 1997, Fractals and Chaos in Geology and Geophysics (CUP)
Vincent, J. B., Oklay, N., Marchi, S., Hoefner, S., & Sierksl, H. 2014, Planet. Space Sci., submitted
Vincent, J.-B., Bodewits, D., Besse, S., et al. 2015, A&A, submitted
Wu, Q., Barkovee, M., & Sticher, H. 1993, Soil Sci. Soc. Am., 57, 883

[1] Center of Studies and Activities for Space, CISAS, G. Colombo, University of Padova, via Venezia 15, 35131 Padova, Italy
e-mail: maurizio.pajola@gmail.com, maurizio.pajola@unipd.it
[2] Max-Planck-Institut für Sonnensystemforschung, Justus-von-Liebig-Weg, 3 37077 Göttingen, Germany
[3] Institute for Space Science, National Central University, 32054 Chung-Li, Taiwan
[4] Geosciences Department, University of Padova, via G. Gradenigo 6, 35131 Padova, Italy
[5] CNR-IFN UOS Padova LUXOR, via Trasea 7, 35131 Padova, Italy
[6] Department of Physics and Astronomy "G. Galilei", University of Padova, Vic. Osservatorio 3, 35122 Padova, Italy
[7] NAF Osservatorio Astronomico di Padova, Vic. Osservatorio 5, 35122 Padova, Italy
[8] Department of Information Engineering, University of Padova, via Gradenigo 6/B, 35131 Padova, Italy
[9] Physikalisches Institut der Universität Bern, Sidlerstr. 5, 3012 Bern, Switzerland
[10] Scientific Support Office, European Space Research and Technology Centre/ESA, Keplerlaan 1, Postbus 299, 2201 AZ Noordwijk ZH, The Netherlands
[11] Operations Department European Space Astronomy Centre/ESA, PO Box 78, 28691 Villanueva de la Cañada, Madrid, Spain
[12] Aix Marseille Université, CNRS LAM (Laboratoire d'Astrophysique de Marseille), UMR 7326, 13388 Marseille, France
[13] Centro de Astrobiologa, CSIC-INTA, 28850 Torrejon de Ardoz, Madrid, Spain
[14] International Space Science Institute, Hallerstrasse 6, 3012 Bern, Switzerland
[15] Department of Physics and Astronomy, Uppsala University, 75120 Uppsala, Sweden
[16] PAS Space Research Center, Bartycka 18A, 00716 Warszawa, Poland
[17] Institute for Geophysics and Extraterrestrial Physics, TU Braunschweig, 38106 Braunschweig, Germany
[18] Department for Astronomy, University of Maryland, College Park, MD 20742-2421, USA
[19] LESIA-Observatoire de Paris, CNRS, UPMC, Univ. Paris 06, Univ. Paris-Diderot, 5 place J. Janssen, 92195 Meudon Principal Cedex, France
[20] Univ. Paris Diderot, Sorbonne Paris Cité, 4 rue Elsa Morante, 75205 Paris Cedex 13, France
[21] LATMOS, CNRS/UVSQ/IPSL, 11 boulevard d'Alembert, 78280 Guyancourt, France
[22] UNITN, University of Trento, via Mesiano 77, 38100 Trento, Italy
[23] Department of Mechanical Engineering, University of Padova, via Venezia 1, 35131 Padova, Italy
[24] INAF Osservatorio Astronomico di Trieste, via Tiepolo 11, 34143 Trieste, Italy
[25] Instituto de Astrofisica de Andalucia CSIC, Glorieta de la Astronomia, 18008 Granada, Spain
[26] Deutsches Zentrum für Luft- und Raumfahrt (DLR), Institut für Planetenforschung, Rutherfordstrasse 2, 12489 Berlin, Germany
[27] Solar System Exploration Research, Virtual Institute, Southwest Research Institute, Boulder, CO 80302, USA
[28] Institut für Datentechnik und Kommunikationsnetze der TU Braunschweig, Hans-Sommer-Str. 66, 38106 Braunschweig, Germany